

Dynamics, stratigraphy and proximal dispersal of supraglacial tephra during the ice-confined 2004 eruption at Grímsvötn Volcano, Iceland

T. C. Jude-Eton · T. Thordarson · M. T. Gudmundsson · B. Oddsson

Received: 2 September 2010 / Accepted: 11 February 2012 / Published online: 8 March 2012
© Springer-Verlag 2012

Abstract The basaltic, phreatomagmatic eruption of Grímsvötn volcano, Iceland, in November 2004 (G2004) lasted for 5 days, during which time two separate vents were active. Significant deposition of tephra occurred in the first 45 h only. We have subdivided the deposit into seven units (A–G) on the basis of differences in texture, grain size and componentry, and the presence of sharp contacts between the layers. The distribution of tephra lobes was used to infer the vent of origin for each unit. The G2004 deposit is poorly sorted overall and consists of non-vesicular to highly vesicular juvenile components. Units A and B comprise almost exclusively non- to poorly vesicular glass fragments, whereas units C–G contain at least 30 vol.% highly vesicular pumice. The proportion of non-juvenile fragments increases significantly in the final unit (unit F) of the main phase; non-juvenile fragments are restricted to the coarse ($>0 \Phi$) fraction of the deposit. Main phase units C and E account for 80% of the total deposit volume, including the entire distal portion, and are interpreted to represent a mixture of (1) a widely dispersed component that fell from the upper margins of a strongly inclined ($\sim 45^\circ$), 6–10 km high plume and (2) a locally dispersed (<3 km from source) component originating from pyroclastic density currents and minor tephra jets.

Keywords Grímsvötn · Glacio-volcanism · Tephra dispersal · Phreatomagmatic · Basalt · Explosive eruption

Introduction

Historical records, along with reconstructions from the geological record, demonstrate that three quarters of all eruptions in Iceland in the postglacial (Holocene) period were explosive (Thorðarson and Höskuldsson 2008; Larsen and Eiríksson 2008). Of these, in the last 1,100 years, over 75% have occurred in a subglacial environment (Larsen 2002). The Grímsvötn central volcano, located in the west–central part of the Vatnajökull glacier (Fig. 1) dominates the event record with, on average, one eruption every 10 years (Larsen et al. 1998).

A typical subglacial to emergent basaltic sequence consists of pillow (or other subaqueously emplaced) lavas overlain by hyaloclastite and phreatomagmatic tephra (e.g. Jones 1966; Skilling 1994; Smellie 2000; Jakobsson and Gudmundsson 2008). In some cases where access to external water becomes restricted, these units may eventually be capped by subaerial lavas (e.g. Jones 1966, 1970). Little attention has been given to supraglacial tephra deposits from such eruptions. Those products are not preserved in situ, implying that the rock record of subglacially constructed volcanic edifices is incomplete. However, in the study of contemporary eruptions, and for more complete understanding of deposits and possible effects of past eruptions, such supraglacial deposits must be described and interpreted.

The focus of this study is the pristine proximal and medial tephra sequence of the 2004 Grímsvötn subglacial basaltic explosive eruption (hereafter referred to as G2004). The pyroclastic ice cauldron fill within the 2004 crater is capped by a small subaerial tephra cone formed during the

Editorial responsibility: J. McPhie

T. C. Jude-Eton (✉) · T. Thordarson
School of GeoSciences, University of Edinburgh,
Grant Inst., Kings Buildings, W. Mains Road,
EH9 3JW Edinburgh, UK
e-mail: t.c.judeeton@gmail.com

M. T. Gudmundsson · B. Oddsson
Institute of Earth Sciences, University of Iceland,
Sturlugata 7,
IS-101 Reykjavík, Iceland

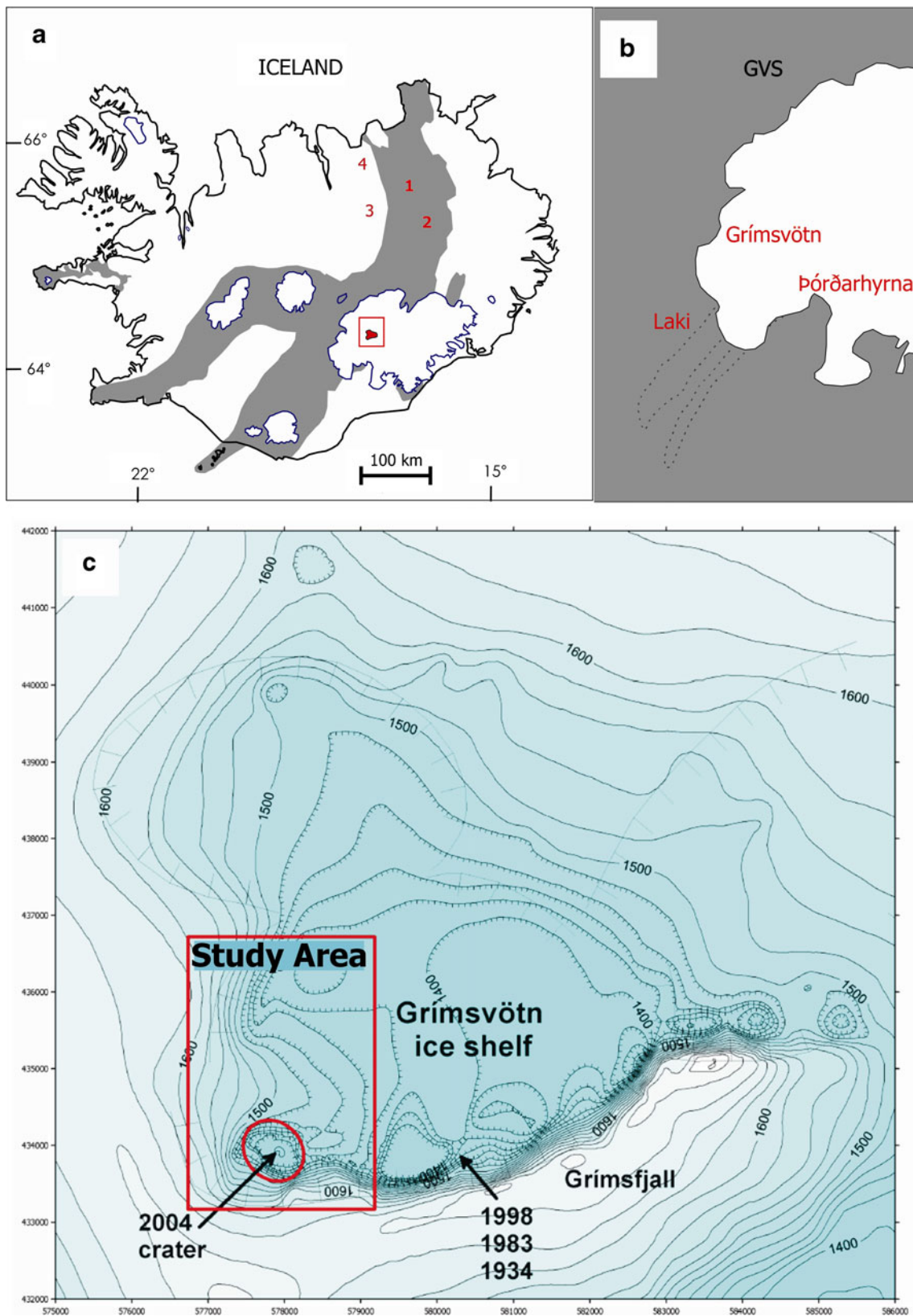


Fig. 1 **a** Map of Iceland showing the location of the Grímsvötn central volcano (*red*) and locations of recorded distal tephra fall (1 Möðrudalur, 2 Grímsstaðir, 3 Svartákot, 4 Reykjadalur). **b** Location and geometry of the key features of the Grímsvötn volcanic system in western

Vatnajökull (modified after Thordarson and Self 1993). **c** Ice surface contours within the Grímsvötn caldera showing the vent locations of G2004 and the twentieth century eruptions. The study area is outlined with a *red box*

waning stages of the eruption (Fig. 2g, h). This tephra cone is equivalent to the bedded tuff sequences at the top of classical subglacial successions. We describe the temporal evolution of the G2004 eruption in light of contemporary visual observations, the detailed tremor record of the event and post-eruption tephra studies. Such a complete study is rarely possible for most glacio-volcanic sequences. We also assess the eruption in the context of our wider understanding of basaltic phreatomagmatic events.

Structure and size of Grímsvötn volcano

The Grímsvötn volcanic system consists of two central volcanoes and an associated fissure system (Fig. 1b). Grímsvötn and the smaller Þórðarhyrna central volcano are aligned along a northeast–southwest trending fissure system (Gudmundsson and Högnadóttir 2007). Grímsvötn is the dominant of the two and is situated at the location of the highest rate of magma supply along the system. Fissure eruptions of the Grímsvötn system include the subglacial Gjálp eruptions in 1938 and 1996 (Gudmundsson et al. 2004) and the infamous 1783–1985 Laki eruption (Thordarson and Self 1993). Grímsvötn contains a 50 km² composite caldera at 1,060–1,200 m above sea level (asl) that consists of three smaller structural domains—the main (or southern), northern and eastern calderas (Sæmundsson 1982; Gudmundsson 1989; Gudmundsson and Milsom 1997). The southern caldera is underlain by a low density, low seismic velocity interval extending to approximately 2 km depth, which is interpreted as subsided and remobilized unconsolidated clastic facies. Gravity and magnetic surveys (Gudmundsson 1989; Gudmundsson and Milsom 1997), along with a teleseismic study (Alfaro et al. 2007), indicate the existence of a shallow magma chamber in the upper crust beneath the volcano.

Grímsvötn is also a very powerful geothermal area and has had a heat output of 2,000–4,000 MW averaged over several decades (Björnsson 1988; Björnsson and Guðmundsson 1993). The geothermal activity beneath the Vatnajökull ice cap has created a depression in the ice surface approximately 10 km in diameter which is bordered to the south by the steep cliffs marking the southern caldera wall at the Grímsfjall ridge. Ice flows into the depression from the west, north and east. This intense geothermal energy release is responsible for the creation and maintenance of subglacial lakes and also affects the extent to which these lakes can be contained by the surrounding ice. Grímsvötn is a renowned source of jökulhlaups, which occur when the level of its subglacial caldera lake reaches an elevation sufficient for meltwater to force its way under the glacier, leading to a drop in lake level of 60–130 m and partial draining of

the lake. Such jökulhlaups have occurred on average once every 4–6 years for most of the twentieth century (e.g. Björnsson 2003).

Eruptions in Grímsvötn

Most eruptions from the central volcano occur along the southern caldera fault where the Vatnajökull ice is 50–200 m thick. Some eruptions have broken through the ice cover almost instantly as magma reached the glacier bed (e.g. the 1998 eruption; Gudmundsson 2005). However, in the 2004 eruption, magma took almost half an hour to melt through 150–200 m of ice in the southwestern corner of the caldera.

In contrast to fissure eruptions under thick ice, as in Gjálp in 1996, melting of ice in a typical Grímsvötn caldera eruption is often quite limited. For example, during the 1998 and 2004 eruptions, only 0.1 km³ of ice was melted. Neither of these eruptions caused major jökulhlaups. Many eruptions (e.g. 2004 and potentially some others in the nineteenth and early twentieth centuries; Albino et al. 2010) were triggered by depressurisation in response to falling lake levels during drainage by periodic jökulhlaups (Thorarinsson 1953; Gudmundsson 2005). This pattern supports the notion of the existence of a shallow-level magma chamber beneath Grímsvötn. Numerical calculations by Albino et al. (2010) confirmed that jökulhlaup-related decompression can trigger eruptions, but only if the underlying magma chamber is already close to erupting because the difference between the tensile strength of the host rocks and the magma pressure at the chamber wall is relatively small.

When eruptions at Grímsvötn are large enough to melt through to the ice surface, the resulting subaerial activity is generally phreatomagmatic in nature and involves large volumes of water provided by melting ice. Eruptions in Grímsvötn typically produce tephra volumes between 0.01 and 0.5 km³ dense rock equivalent (DRE; Thorarinsson 1974; Björnsson and Guðmundsson 1993; Gudmundsson 2005; Thordarson and Larsen 2007) and last for several days to a few weeks. An island usually forms within the ice-confined lake (ice cauldron), along with a tephra fan extending onto the ice cap downwind from the eruption site. Tephra fallout from these events seldom extends beyond Vatnajökull (Larsen et al. 1998; Thordarson and Larsen 2007; Thorðarson and Höskuldsson 2008).

The high frequency of Grímsvötn eruptions compared with elsewhere in Iceland, along with the cyclic nature of this activity, can be attributed to the proximity of the volcano to the centre of the Iceland mantle plume (Wolfe et al. 1997). Larsen et al. (1998) showed that in historical time (i.e. the past 1,100 years), there have been over 70 eruptions attributed to Grímsvötn and that this activity

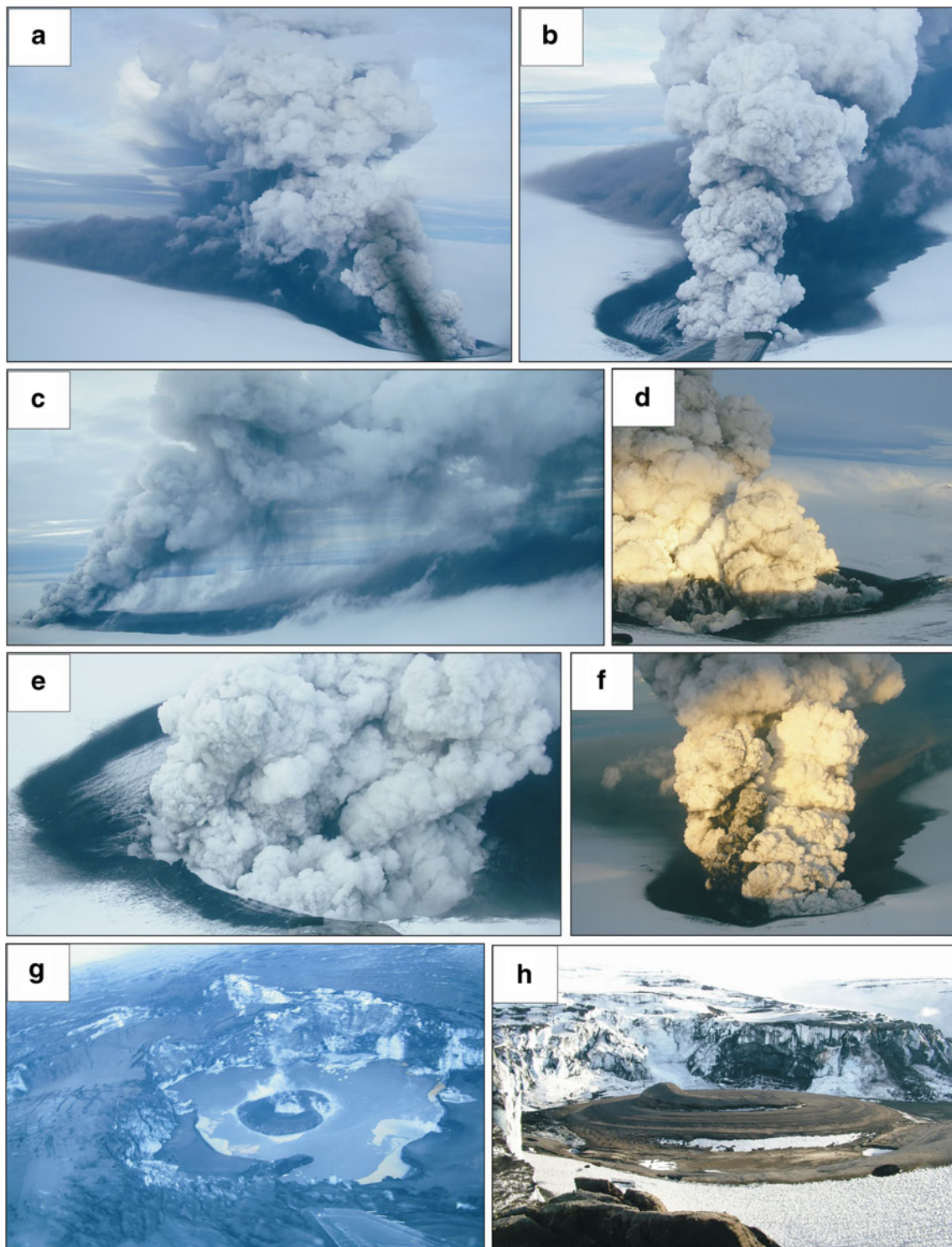


Fig. 2 Photo time series of activity towards the end of the main phase of the eruption—all pictures (except bottom row) taken 02 November 2004. **a** (15:34) Eruption plume and pyroclastic density currents viewed from the southwest. **b** (15:35) PDC and plume viewed from the south. Note the narrowly confined and clearly delineated boundary of deposits. **c** (15:38) Pyroclastic fallout viewed from the northeast. Note that the plume is strongly inclined towards the north, due to strong southerly winds. **d** (15:56) View from the southwest. Observe low-level jets emitted from two distinct vents. **e** (15:40) View from the

south. Note that the southern and western sides of the ice cauldron are confined by steep ice walls. **f** (16:11) View from the south-southwest. At this moment, the western vent dominates activity. Note also that the deposit has a highly irregular outline close to the vent, which narrows and smoothes out in the more distal region. **g** Aerial view towards the southwest of the tephra apron and late-stage tuff cone at the end of the 2004 eruption on November 6. **h** Grímsvötn 2004 tuff cone as preserved in August 2005. View towards the south-southwest

is characterised by 50–80 year-long alternating cycles of high vs. low eruption frequency.

Despite Grímsvötn's remote location, significant hazards are posed by eruption-generated jökulhlaups. In addition, ash-laden eruption plumes pose a hazard for air traffic in the North Atlantic (cf. the 2010 eruption at Eyjafjallajökull Gudmundsson et al. 2010; Schuman et al. 2010; Davies et al. 2010), so the characterisation and anticipation of these events is a high priority.

Chronology of the 2004 eruption

The G2004 eruption is the best documented volcanic event at Grímsvötn, both in terms of geophysical measurements and visual observations (Vogfjörð et al. 2005; Sigmundsson and Guðmundsson 2004). The Icelandic Meteorological Office (Veðurstofa Íslands, hereafter referred to as IMO) weather radar is located on the Reykjanes Peninsula 260 km away from Grímsvötn. During volcanic eruptions, radar images are acquired every 5 min. Due to the distance to the radar station, the beam width above Grímsvötn is 4 km and the detected plume altitudes are therefore averaged over this vertical distance. The IMO also operates a nationwide digital seismic network along with a network of continuous GPS stations (ISGPS) to monitor seismic and volcanic activity in Iceland. The instrument records used in this study were collected from these sources (Vogfjörð et al. 2005).

The 2004 eruption had been anticipated for several months, as abundant data recording precursory activity at the site were available prior to the event. A jökulhlaup from Grímsvötn commenced on October 28; and by November 1, the water level in the caldera lake had fallen by 15 m. Frequent earthquakes were recorded on November 1 and an intense swarm between 20:20 and 21:50 marked the progress of magma upward to the base of the glacier.

G2004 commenced as a subglacial event located in the southwestern corner of the Grímsvötn caldera at 21:50, as indicated by the onset of continuous tremor. Within half an hour, magma melted through ice almost 200 m thick to erupt subaerially, forming an approximately 750-m long and 550-m wide ice cauldron over the next 2 days. The eruption plume was detected by the IMO weather radar at 22:50 UTC and at that time had already risen to 6 km above the vent. Over the following 4 h, the plume increased to 10 km above the vent (Sigmundsson and Guðmundsson 2004). The seismic tremor activity was high for the first 24 h, and then tremor amplitude slowly declined for the next 21 h, after which it fell to background levels (Fig. 3). The record is punctuated by several higher-amplitude pulses in the early evening of November 2 and also the following morning. Visual inspections from aircraft revealed that, at times, two distinct vents were simultaneously active and pyroclastic

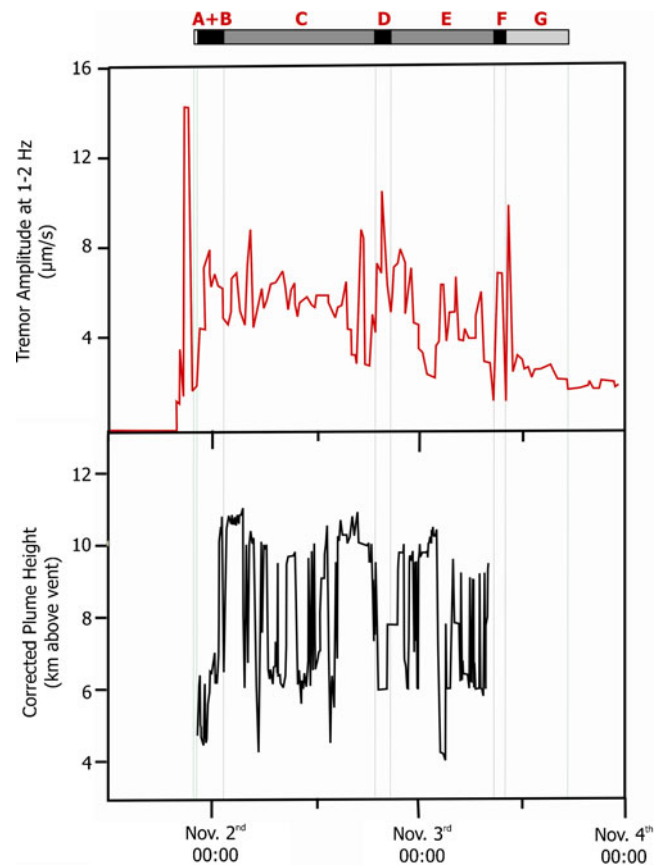


Fig. 3 Tremor amplitude and corrected IMO radar plume height records (modified from Vogfjörð et al. 2005) correlated with deposit stratigraphy to identify the duration and intensity of activity associated with each unit. On the bar at the top, periods of quiescence are represented by *white*, short, high intensity bursts by *black*, sustained deposition by *dark grey*, and low intensity PDC activity by *pale grey*. The start of the eruption, beginning of the subaerial phase, and end time of significant tephra deposition are demarcated by thin *green lines*

density currents (PDC) occurred concurrently with fallout from a high eruption column (Fig. 2a, b).

On November 2, vigorous continuous uprush alternated with less energetic explosivity, and the plume oscillated between altitudes of 6 and 10 km above the vent (Oddsson 2007). The ejection of intermittent tephra jets (also known as cypressoidal or rooster-tail jets) was also observed, although this component of the activity was minor. The terms “continuous uprush” and “rooster-tail jets” were coined by Thorarinnsson (1964) to describe two distinct eruption styles observed in the emergent phases of the 1963–1967 Surtsey eruption, each driven by copious tephra-rich phreatomagmatic explosions on the time scale of seconds to minutes. Rooster-tail jets occur where water has ready access to the vent and originate from multiple shallow explosions, each producing vertical to sub-horizontal black tephra jets. Continuous uprush events take place where the vents are completely surrounded by tephra walls, thus restricting the access of water, and can last for hours. The continuous

uprush events originate from explosions rooted deeper in the vent, which produce vertical 0.5–2 km high, black tephra-rich columns with muzzle velocities $>100 \text{ ms}^{-1}$ and maintain convective eruption columns rising as high as 12 km. The continuous uprush events are normally more powerful than the rooster-tail jets because of the lower water to magma mass ratio.

The G2004 eruption plume was pushed northwards by strong southerly winds, shifting towards the north–northeast in the afternoon. The fallout was principally towards north–northeast on November 2 but towards the north on November 3 (Oddsson 2007). Tephra fall was observed at manned weather stations in northeastern Iceland on November 2 and 3. The distal fallout was relatively minor. It did not form a continuous layer on the ground and was observed only for limited periods at each station. The jökulhlaup initiated on October 28 reached its peak flow of over $3,000 \text{ m}^3\text{s}^{-1}$ on the afternoon of November 2. Nevertheless, diminished flow persisted until early in December 2004 (Vogfjörð et al. 2005).

The IMO radar cannot detect plumes lower than 4 km asl (i.e. approximately 2 km above the vent) due to the curvature of the Earth. At 08:30 on November 3, the plume fell out of radar view and the last high-amplitude tremor recorded was at 10:54. Tephra production at this time was minor. From the afternoon of November 3, activity was characterised by intermittent phreatomagmatic explosions (Sigmundsson and Guðmundsson 2004; Vogfjörð et al. 2005). On November 4, a weak plume was observed from aircraft to extend 1.5–2 km above the vent. This plume produced a thin deposit extending a few kilometres to the east, which accounts for only a fraction of a percent of the total tephra produced. Thus, almost all of the deposits produced by the G2004 event are contained within the main, north-directed tephra sector. The tephra fall deposit from the eruption is therefore very well defined, extending north and north–northeast from the vent. On November 6, the last explosion signal was detected at the Grímsfjall seismic station. By the end of the eruption, a tephra ring approximately 200 m in diameter had formed within the ice cauldron.

Methods

Study of proximal units

The G2004 tephra layer was very well preserved on the glacier in the months and years following the eruption. Aeolian and water erosion is largely absent at the surface of the accumulation areas of glaciers, allowing for accurate sampling and mapping of tephra layers until they are buried by subsequent snowfall. Eventually, ice flow transports the tephra from the accumulation areas to ablation areas leading to gradual removal of the tephra layer. In Iceland, this

process occurs on a time scale of 100–1,000 years (Larsen et al. 1998) while in colder, larger and less dynamic glaciers, it may be much longer.

Isopach maps based upon field data were constructed for single units using ArcGIS. The total deposit thickness is better constrained than that of single units and so the total deposit map was used as a constraint on the sum of single unit thicknesses. Thinning trends were determined from a semi-log plot of $(\text{area})^{1/2}$ vs. thickness (after Pyle 1989). For comparison, the data are also presented in the more traditional form of distance vs. thickness plots. We measured the average linear thickness half-distance ($t_{1/2}$) for the bulk deposit and its units. The parameter $t_{1/2}$ is defined as the measured distance over which the deposit halves in thickness along any single transect and can be measured in both radial and tangential transects with respect to the vent (Houghton et al. 2004).

Although not a conventional application, we describe the G2004 deposit according to the $(\text{area})^{1/2}$ vs. thickness plot and $t_{1/2}$ parameter across all units regardless of their interpreted origin. This application is justified because (1) it provides a means of looking at how the deposit thickness changes with distance in a manner that is consistent across all units (especially the hybrid fall–PDC units) and (2) the entire proximal–medial succession was deposited on a relatively flat glacier surface, so no complications arise from topographic influence. It is given that this method cannot be used to extract volumes for PDC deposits without substantial error, and that we cannot relate these parameters to changing depositional regimes in PDC emplacement. Nevertheless, it allows for exploration of the general changes in PDC and hybrid unit thicknesses with distance from the vent and evaluation of how these changes are fundamentally different from those of conventional fall deposits.

The deposit volume has been obtained by direct integration of the unit and total thickness isopach maps, a method shown to be valid for calculating deposit volume or mass in cases where the tephra blanket is well preserved and/or samples are collected shortly after the eruption (e.g. Carey and Sparks 1986; Pyle 1989; Fierstein and Nathenson 1992). For the proximal area, where the layer is thick and continuous, direct measurements of thickness were used, whereas for the distal region mass per unit area values were converted to thickness using the average measured density of the deposit ($1,190 \text{ kg m}^{-3}$; Oddsson 2007). The volume of magma erupted was calculated using a magma density value of $2,750 \text{ kg m}^{-3}$ (Metrich et al. 1991).

Grain size sampling technique and sieving

Bulk representative samples of whole units and single sub-layers were carefully collected from the top-down of each section in order to avoid cross-contamination between

layers. The samples were then dried for 24 h in an oven set to 60°C before being divided into four representative portions using a riffle-type sample splitter.

Granulometric analyses of 230 bulk tephra samples were performed using a combination of hand sieving and Coulter Counter techniques. One portion of the divided sample was sieved by hand to 5Φ at 0.5Φ intervals, whereas another portion was sieved to remove all fragments larger than 1Φ . A deflocculant was added to this fraction to allow particle size analysis to be performed using a Beckmann Coulter LS230, housed at the Department of GeoSciences, University of Edinburgh. Size intervals common to the two methods allowed the datasets to be merged to create a continuous tephra size distribution from -6Φ to 10Φ .

Inman (1952) parameters are used to express grain size characteristics (Md_{Φ} , median diameter = Φ_{50} ; σ_{Φ} , sorting = $[\Phi_{84} - \Phi_{16}]/2$) along with Folk and Ward's (1957) inclusive skewness parameter ($Sk_I = ([\Phi_{16} + \Phi_{84} - 2\Phi_{50}]/2(\Phi_{84} - \Phi_{16})) + [\Phi_5 + \Phi_{95} - 2\Phi_{50}]/2(\Phi_{95} - \Phi_5)$) and graphic kurtosis ($K_G = (\Phi_{95} - \Phi_5)/2.44(\Phi_{75} - \Phi_{25})$).

Correlation of eruption units with seismic tremor amplitude

The seismic tremor data provide a continuous record relating to the eruption (Vogfjörð et al. 2005). The parameters that control tremor amplitude are not fully constrained but in many eruptions, a correlation exists between eruption magnitude and tremor magnitude (e.g. McNutt and Nishimura 2008). Acknowledging that a number of parameters may affect tremor behaviour, we attempt here to correlate the onset of deposition of single proximal eruption units with spikes in tremor amplitude and corresponding changes in plume altitude. For example, a change from a period of sustained combined PDC and fall activity, to PDC-dominated activity could correlate with a spike in tremor amplitude and a sudden drop in plume height.

Eruption parameters

Deposit mass and volume

Extensive tephra sampling was undertaken in the summers of 2005 and 2006 on the Vatnajökull glacier and the ice-free region to the north, covering the area of detected tephra fallout (Oddsson 2007; this study). The tephra blanket in the distal sector was relatively thin (<3 cm) and thus subjected to substantial reworking by ablation, surface runoff and wind in the summer of 2005. However, the proximal to medial sectors of the tephra deposits are situated on the high glacier and thus not affected by these secondary processes induced by the seasonal cycles. During this time, ice movement towards the crater resulted in crevasse formation

which provided profiles through the otherwise undisturbed tephra succession in the proximal to medial sectors.

The total mass of the deposit is found to be $5.6 \pm 1.0 \times 10^{10}$ kg. Seismic refraction measurements show that the tephra pile in the ice cauldron is 70 m thick, containing $2.7 \pm 0.5 \times 10^{10}$ kg (Oddsson 2007). The total mass of tephra outside the cauldron (proximal and distal) is $2.9 \pm 0.5 \times 10^{10}$ kg. The corresponding DRE volumes are $4.7 \pm 0.8 \times 10^7$ m³ for the total deposit, $2.3 \pm 0.4 \times 10^7$ m³ for the tephra within the ice cauldron and $2.4 \pm 0.4 \times 10^7$ m³ for the proximal and distal tephra (Table 1).

Ice cauldron development

The development of an ice cauldron was an important part of the G2004 eruption since the cauldron contains about 50% of the erupted material and its formation accounts for about one third of the total thermal energy released (Gudmundsson et al. 2009). Observations of the cauldron at 10:24 and 16:00 on November 2 and later (e.g. from the ground on November 4 and the air on November 7) allow its size to be estimated. At 10:24 on November 2, the length of the cauldron was close to 650 m and the maximum width was around 400 m. At 16:00, it was approximately 700 m long and 500 m wide. The values recorded on November 7 were 750 and 550 m. Assuming that the cauldron was elliptical, these numbers indicate that the cauldron had already reached 65% of its final size at 10:24 on November 2 and 85% by 16:00. It is likely that by the end of the main activity on November 3, the cauldron had reached a size very close to that of November 7. These numbers can be translated into filling rates, assuming that a 70 m thick pile of pyroclasts accumulated in a cauldron with vertical or sub-vertical ice walls. That is, at 10:24 on November 2, 65% of the cauldron fill volume had been formed, 85% at 16:00 and almost 100% by the afternoon of November 3. Using a density of $1,190$ kg m⁻³ for the cauldron fill, a total fill of mass 2.7×10^{10} kg and DRE density of $2,750$ kg m⁻³, the filling rates (m³s⁻¹; Fig. 4) can be calculated. Two simplified models are shown, both assuming a linearly declining filling rate with time. One model assumes a cauldron filling time of 45 h (corresponding to the total duration of deposition) and the other only 36 h (corresponding roughly to the duration of a high eruption plume only). The shorter filling time fits the observational data better and is therefore used to determine the contribution of each unit to filling the ice cauldron (Fig. 4).

Proximal–medial tephra stratigraphy

Detailed logging and stratigraphic correlation of 59 vertical sections through the proximal tephra succession to the north of the vents reveals that it consists of a distinctly bedded sequence representing three separate phases of activity

Table 1 Key eruption parameters for single units, and the whole G2004 deposit

Unit	Volume (10^6 m ³)	DRE volume (10^6 m ³)	Mass (10^9 kg)	Proportion of proximal deposit	Proportion of subaerial deposit	$t_{1/2}$ (m)	Mass of tephra in ice cauldron (10^9 kg)	Distal mass (10^9 kg)	Total mass (10^9 kg)
Subglacial									
A	0.59±0.10	0.26±0.03	0.71±0.09	3.7%	2.4%	490 m	0.6±0.2	0	0.6±0.2
B	1.47±0.17	0.64±0.07	1.76±0.21	9.4%	6.1%	490 m	4.4±0.8	0	6.9±1.1
C	7.59±0.91	3.31±0.37	9.11±1.10			1.52 km (average)			
				47.8%	54.4%	520 m (proximal)	17.5±3.0	5.8±2.0	32.4±6.1
D	0.88±0.11	0.38±0.04	1.06±0.13	5.6%	3.7%	290 m	1.0±0.3	0	2.1±0.4
E	3.73±0.45	1.63±0.19	4.48±0.54			1.63 km (average)			
				23.6%	26.8%	190 m (proximal)	3.5±0.7	4.2±1.0	12.2±2.2
F	0.52±0.06	0.23±0.03	0.62±0.11	3.2%	2.1%	5.96 km (distal)	0	0	0.6±0.1
G	1.08±0.13	0.47±0.06	1.30±0.26	6.9%	4.5%	190 m	0	0	1.3±0.3
						400 m			
Sum of units (proximal)	1.59 (±0.19)×10 ⁷	6.92 (±0.79)×10 ⁶	1.90 (±0.23)×10 ¹⁰						
Total cauldron mass	2.3 (±0.4)×10 ⁷	1.0 (±0.2)×10 ⁷	2.7 (±0.5)×10 ¹⁰						48%
Total proximal mass	1.6 (±0.2)×10 ⁷	0.7 (±0.1)×10 ⁷	1.9 (±0.2)×10 ¹⁰						34%
Total distal mass	0.8 (±0.2)×10 ⁷	0.4 (±0.1)×10 ⁷	1.0 (±0.3)×10 ¹⁰						18%
Total	4.7 (±0.8)×10 ⁷	2.1 (±0.4)×10 ⁷	5.6 (±1.0)×10 ¹⁰			650 m			

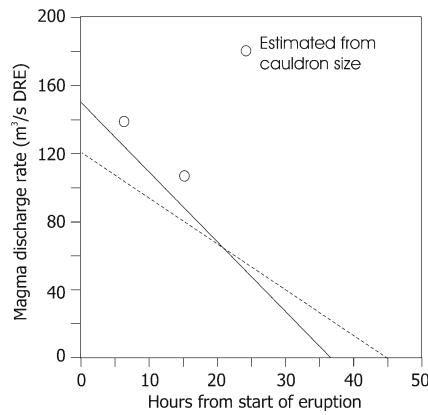


Fig. 4 Calculated filling rate of the ice cauldron using a density of $1,190 \text{ kg m}^{-3}$ for the cauldron fill, a total fill of mass $2.7 \times 10^{10} \text{ kg}$ and DRE density of $2,750 \text{ kg m}^{-3}$. Both models shown assume linear decline in filling rate with time. The *dashed line* assumes a cauldron filling time of 45 h (the total duration of identified phases to the north of the vents). The *solid line* assumes 36 h (the duration of high eruption plume). The curve generated by applying the shorter duration provides a better fit to observations of cauldron size over time

(Table 2). Seven units, labelled A–G, are identified within the proximal to medial sector of the 2004 deposit. Units A and B originated from the eastern vent and were deposited during the initial phase of the eruption, whereas the main phase (i.e. units C–F) was a period of sustained deposition. At the start of this main phase, both vents were active. However, after the deposition of unit D, activity was re-established at the western vent only. During waning activity only one unit (unit G) was deposited north of the vents. Only the eastern vent was observed to be active during the waning stages of the eruption. Although minor fallout of tephra occurred to the east and south after November 3, the deposits from this late activity form a very thin (1 mm) layer. They represent a fraction of a percent of the total deposit and are not considered further here.

Proximal, medial and distal regions—definitions

The main tephra sector trends north to north–northeast across the glacier as a result of southerly winds during the eruption. At a distance of 50 km from the eruption site, near the northern edge of Vatnajökull, the layer is 30 km wide. The delineation of proximal, medial and distal areas within the deposit is based on the thinning–distance curve generated from the total thickness isopach map (Fig. 5a). Due to over-thickening in the vent area, syn-eruptive remobilisation of tephra and rising lake levels, the area representing the ice cauldron has been removed from the curve.

A clear inflection point is observed at 4.0 km, delineating the distal (>4 km) and medial regions of the deposit. Another occurs between 1.9 and 2.4 km from source. We have therefore arbitrarily defined 2.3 km as the boundary between the proximal and medial deposit. On either side of these inflection points (2.3 and 4.0 km), the curve is defined by different exponential trends, which form four or more straight-line segments on a semi-log thickness distance plot (Fig. 6b).

Unit descriptions and interpretation

We refer to clasts with >60 vol.% vesicles as pumice, whereas clasts in the range of 20–60 vol.% vesicles are called scoria. Pumice of the same composition as scoria will generally appear paler in colour, primarily because vesicle walls are thin in pumice (1–10 μm) and thick (>10 μm) in scoria. We refer to transparent pale brown to brown basaltic glass as sideromelane, whereas dark brown to black, opaque “glass” is called tachylite. In the G2004 deposit, tachylite contains >10 vol.% micro- or crypto-crystals. Juvenile fragments consist exclusively or dominantly of glass and exhibit

Table 2 Key features and interpretations of each depositional unit and the corresponding G2004 eruption phases

Unit	Dispersal	Key features and interpretation	Subaerial eruption phase
A	Moderate. Issued from the E vent, directed N	Tephra fallout. Dense, blocky, exclusively juvenile clasts	1
B	Issued from the E vent, dispersed in all directions. Irregular outline due to lobe-by-lobe emplacement	Dilute PDC. Dense, blocky, exclusively juvenile clasts	1
C	Extensive, directed N to NNE. Both vents active	Combined fall and PDC. Abundant, distinctive pumice “lenses” and “trains”	2
D	Issued from both vents, consists of two distinct lobes—one directed to the NNW and one to NE	Dilute PDC. Finely laminated, pinch-and-swell morphology. Varying proportions of dense, blocky clasts and bubble-wall shards. Some non-juvenile clasts	2
E	Issued from the W vent, directed N. Similar in geometry to unit C, but more narrowly confined lateral extent	Combined fall and PDC. Higher proportion of pumice “trains” relative to “lenses” than in unit C	2
F	Issued from the W vent, directed E. Confined to the proximal area	Directed, partial column collapse event. Poorly sorted, lithic-rich, fines abundant	2
G	Consists of two lobes. May have issued from both vents, only the E vent was active towards the end of the eruption	Pumice-rich PDC. Fines-rich, armoured clasts and accretionary lapilli	3

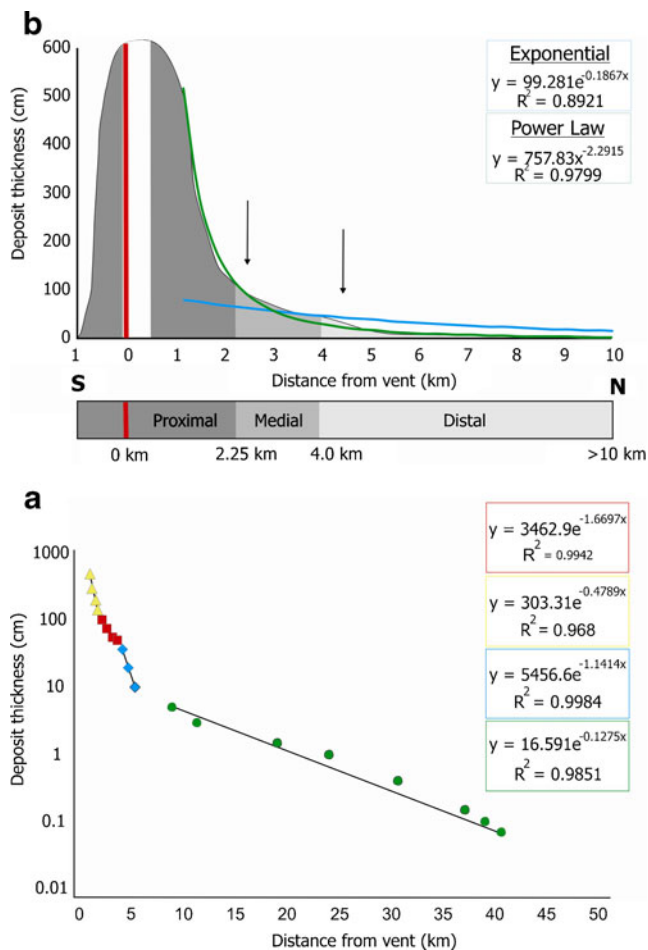


Fig. 5 **a** Deposit thinning profile generated from the total thickness isopach map. The area representing the ice cauldron is not shown. The blue line is the line of best fit for an exponential thinning trend and the green line gives the best fit power law trend. The power law thinning trend provides the better fit (R^2 value closer to 1). **b** A semi-log thickness–distance plot, equations of best fit and the corresponding R^2 values

a range of morphologies. Non-juvenile components are easily distinguishable from juvenile clasts in that they consist of primarily of blocky crystalline lava fragments, although a small proportion (<10 vol.%) are fragments of consolidated hyaloclastite. Furthermore, non-juvenile components are typically hydrothermally altered, oxidised or palagonitized.

UNIT A

Description

Unit A is relatively widespread (Fig. 6) and is found at every location in which the basal contact of the tephra with the ice is exposed. Unit A isopachs extend into the medial region of the deposit. The dispersal axis trends directly northwards and its trace intersects the eastern vent on the 2004 fissure.

Fig. 6 Total deposit (modified from Oddsson 2007) and unit isopach maps. Measured sample locations are indicated by red dots in the first panel and the contour thicknesses are given in centimetres. The dispersal axes of fall-dominated units (C and E) reflect the moderate southerly winds acting throughout the eruption. Tephra dispersal was controlled by the presence of the 300-m-high caldera wall directly to the south of the vents

In the downwind direction, unit A has a maximum measured thickness of 50 cm at 480 m from source, steadily thinning to <1 cm within 3.5 km of the vent (Fig. 7) as it uniformly drapes the ice surface. In the eastern (cross-wind) dispersal area, unit A is 40 cm thick in the most proximal sections, thinning to less than 0.5 cm 2 km farther to the east. The thickness data form two straight-line segments on the semi-log dispersal diagram (Fig. 8), whereby the medial segment (2.5–3.5 km from source) is steeper than the proximal segment. The average $t_{1/2}$ over this interval is 490 m.

Unit A stands out among the G2004 tephra units because it is massive and black, consisting entirely of poorly vesicular, tachylitic, blocky, juvenile pyroclasts. Non-juvenile clasts and highly vesicular fragments are entirely absent. Close to the vent, unit A ranges from fine ash to fine lapilli (Fig. 9), and the median grain size is coarse ash ($Md_{\phi} = 0.80$). The median grain size decreases to medium ash ($Md_{\phi} = 1.10$) beyond a distance of 1.2 km from source. This layer is poorly sorted overall ($\sigma_{\phi} = 2.35$). In almost all cases, it is accompanied by a very thin (millimetre to sub-millimetre) continuous layer of tan brown, very fine ash at the ice contact (Fig. 10). Close to the vent, unit A is also capped by a very fine, tan ash layer.

Unit B

Description

Unit B issued from the eastern vent and was dispersed primarily towards the north and northeast. The deposit has an irregular outline and features a series of at least four radial lobes with dispersal axis orientations ranging from north–northwest to east–northeast (Fig. 6). Single lobes have maximum extents of approximately 3.5 km and are thus largely confined to the proximal and medial region.

Although unit B shows minor changes in lateral thickness when plotted on a dispersal diagram (Fig. 8), localised over-thickening and pinch-and-swell morphology are not evident on the outcrop scale. Within the proximal area, the $t_{1/2}$ value of unit B is identical to that of unit A (490 m).

Units A and B are remarkably similar in composition and clast morphology, but differ vastly in terms of structure and internal fabric (Fig. 10a, b). Unit B is cross-bedded, consisting of a minimum of five, 3.5–5 cm thick, reverse-graded bed sets (from clast diameters of 0.5ϕ at the bottom to -1ϕ

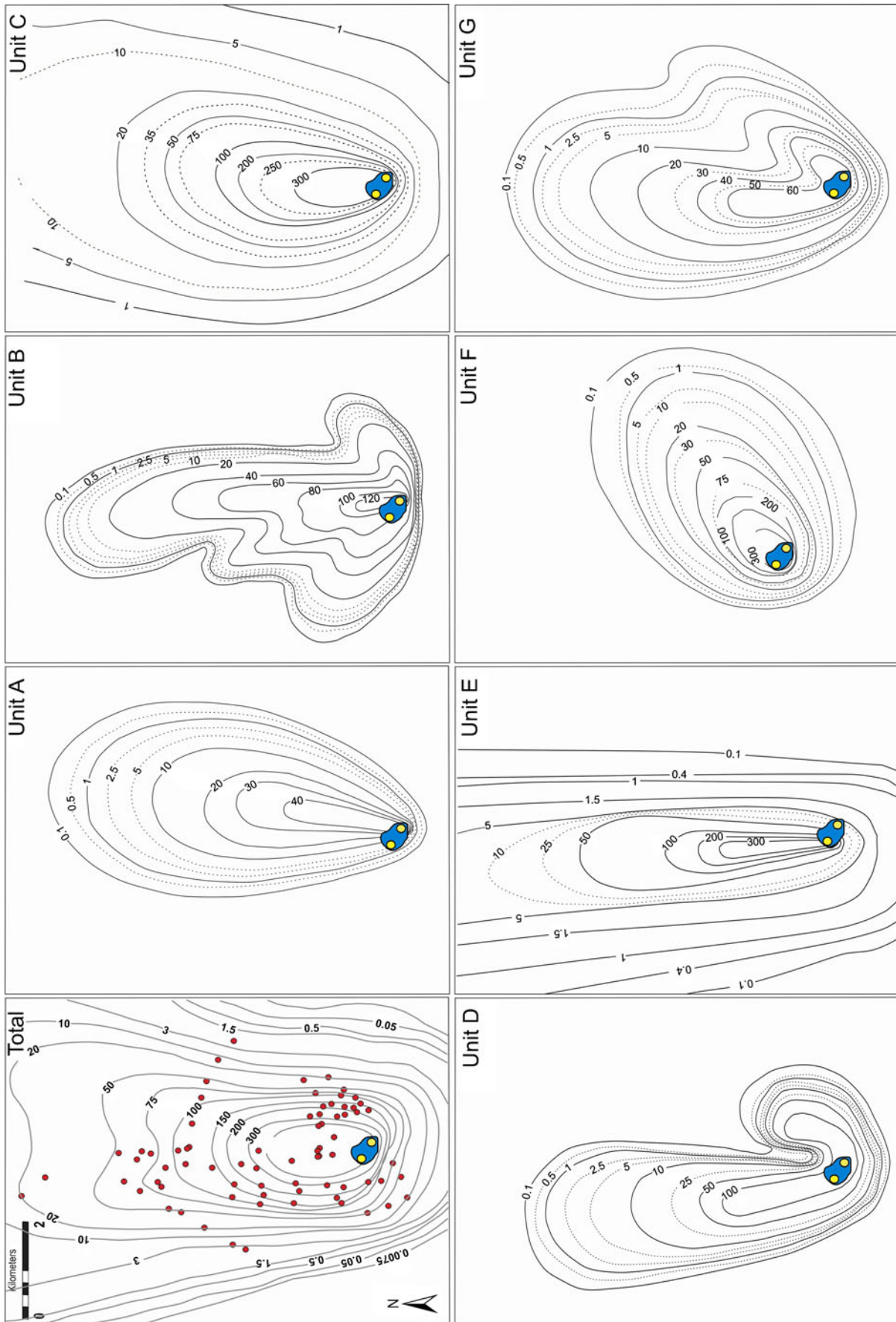
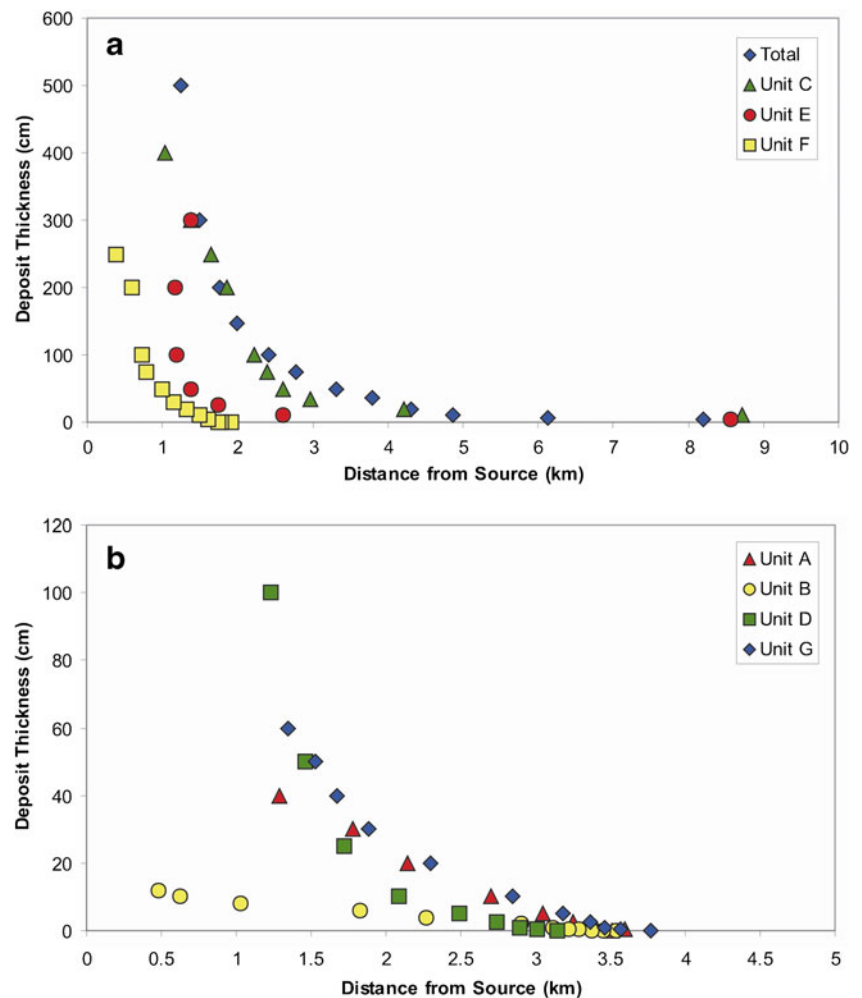


Fig. 7 Simple downwind thinning profiles by unit



at the top), which are capped by laminae of fine ash ($Md_{\phi} = 2.5\text{--}3$). The thickness of laminae within bed sets increases slightly towards the top of the deposit (from 1 mm near the bottom to 3 mm at the top). Representative coarser cross-beds have wavelengths of 56 cm and amplitudes of 3 cm, whereas medium ash layers have a similar wavelength but the amplitude is generally 3.5–5 cm. The median grain size of the entire unit is 1.3Φ . Although single bed sets appear moderately to well sorted, unit B is actually rather poorly sorted overall ($\sigma_{\phi} = 2.40$; Fig. 9). Unit B is distinctively black, although the fine ash layers are grey.

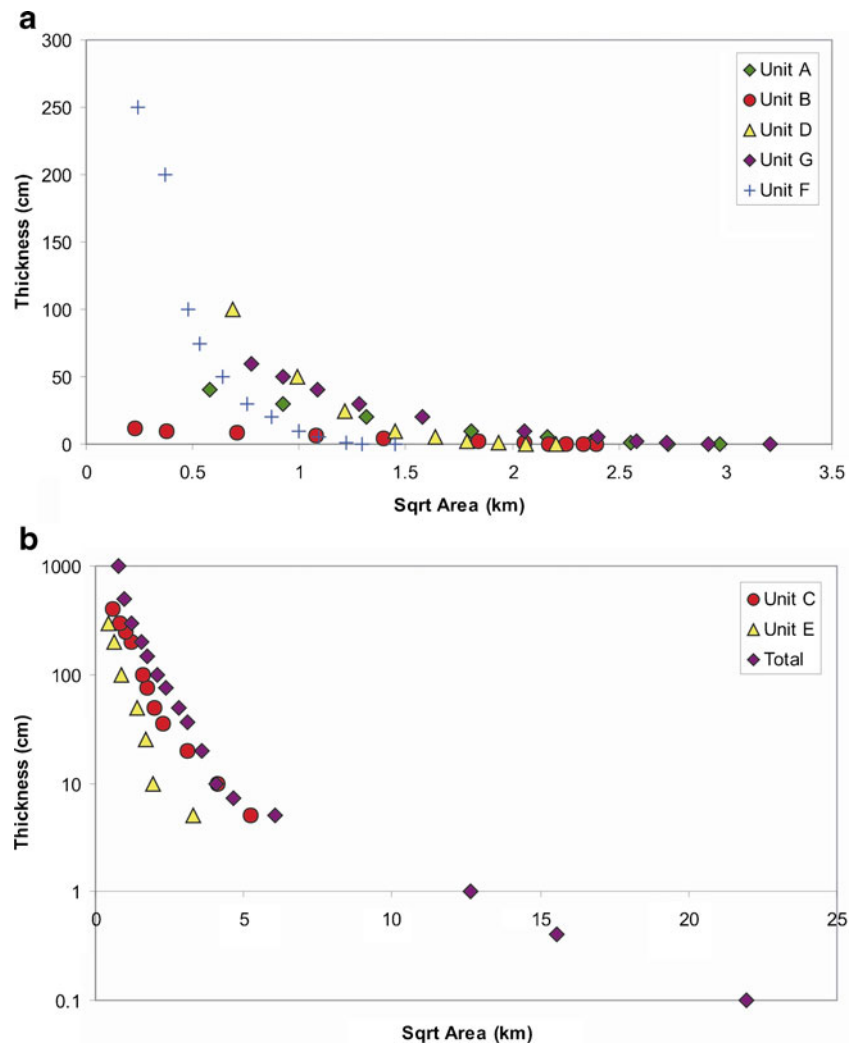
Interpretation of unit A and B deposits

Units A and B record the first subaerial phase of deposition and are similar in terms of components and dispersal. The consistent dispersal pattern of unit A, its uniformly decreasing thickness and massive internal structure indicate that it is a fall deposit. On a plot of median diameter vs. sorting (Fig. 11), unit A samples fall just outside of the sorting field defined by Walker and Croasdale (1972) for fall deposits. This result is likely to be a consequence partly of the

phreatomagmatic origin of this unit (as suggested by the poorly vesicular and blocky nature of its components) and also of the unusually close proximity of sampling to the vent, as all the other characteristics of this unit point to a fall origin. The low $t_{1/2}$ value is consistent with dispersal by moderately explosive activity and thickness data are more consistent with a linear, rather than exponential, thinning trend. By contrast, the distinct lobes of unit B define variable dispersal axes. A simple downwind profile of unit B (Fig. 8) reveals areas of localised over-thickening and pinch-and-swell morphology which are characteristic of dilute (low-concentration) PDC (Sohn and Chough 1989). Coupled with the internal characteristics (reverse grading and fine cross-stratification), the thickness variations indicate emplacement by dilute and closely spaced PDC generated by phreatomagmatic explosions. The increasing thickness of fine ash layers higher in the stratigraphy is consistent with decreased frequency of PDC at the close of the first phase of subaerial activity.

A key feature of these two units is the exceptionally low vesicularity of juvenile pyroclasts compared with the rest of the deposit. The average sulphur content of the groundmass

Fig. 8 Thickness vs. square root of area by unit (after Pyle 1989)



glass is around 800 ppm in juvenile pyroclasts from all units (except the pumice lapilli, for which it is 688 ppm), which implies that the degree of degassing (using 1,670 ppm as a representative value for un-degassed melt inclusions) is around 50% for all units, on average (Table 3). The data therefore show that there is no significant difference in the degassing of unit A and B magma compared to that of later units (Fig. 12) and also that the melt represented by the ash fraction was only partly degassed at the point of disintegration. However, only units A and B are dominated by grains of low to very low vesicularity—other units contain components formed by disintegration of moderately to highly vesicular magma. This relationship implies that the initial batch of melt that rose to the surface lost some bubbles before being disintegrated.

The fact that unit A is massive and everywhere underlies unit B is a strong indication of fallout from a single explosion. Furthermore, the identical $t_{1/2}$ values indicate that the two units were of similar intensity. The smaller volume of unit A (<5% of the proximal part of deposit) compared to that of unit B (~9%) thus implies that eruption of unit A was of shorter duration than unit B (cf. Sable et al. 2006). Tephra fall would

have been continuous and heavy, but of short duration, during the opening of the ice cauldron on the evening of November 1.

Unit C

Description

Unit C is the most widespread unit (Fig. 6), deposited during the main phase of the eruption and accounting for over half the total subaerial deposit (half of proximal, two thirds of distal). It is present in every section of the principal dispersal areas, and the eastern margin has been traced by field observations. The isopachs constructed from field data agree with visual observations on the afternoon of November 2 indicating that the eastern and western vents were simultaneously active when this unit was deposited. It is inferred that tephra deposited in the distal regions of the deposit is temporally correlated to unit C.

Unit C is up to 5 m thick in proximal sections and lateral thickness measurements are quite consistent. There is an

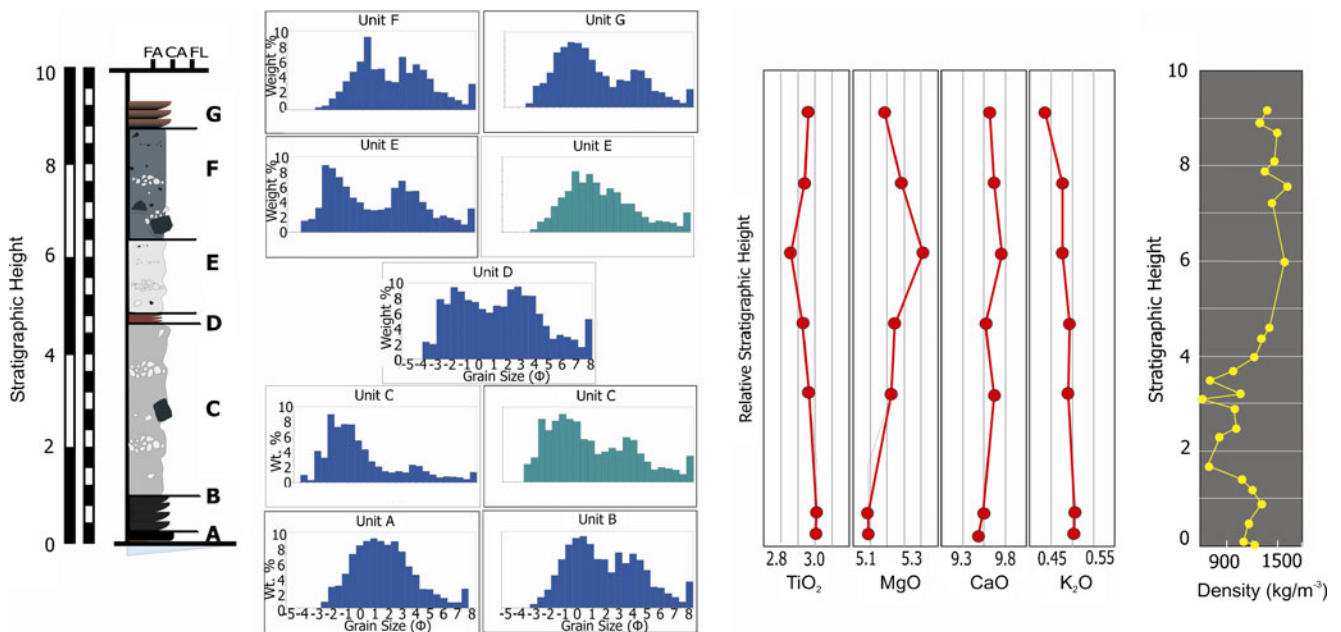


Fig. 9 Stratigraphy of the G2004 deposit at locality TT01 (~550 m northeast of the vent), showing typical unit thicknesses, grain size characteristics, average glass composition and deposit density

inflection point in the thinning profile of this unit at 3 km from the source (Fig. 7). Around this mark, the average $t_{1/2}$ value changes from 520 m to 4.5 km.

Unit C features multiple packages displaying indistinct discordant beds, highlighted by numerous single-grain-thick pumice lapilli trains. These packages are relatively poorly

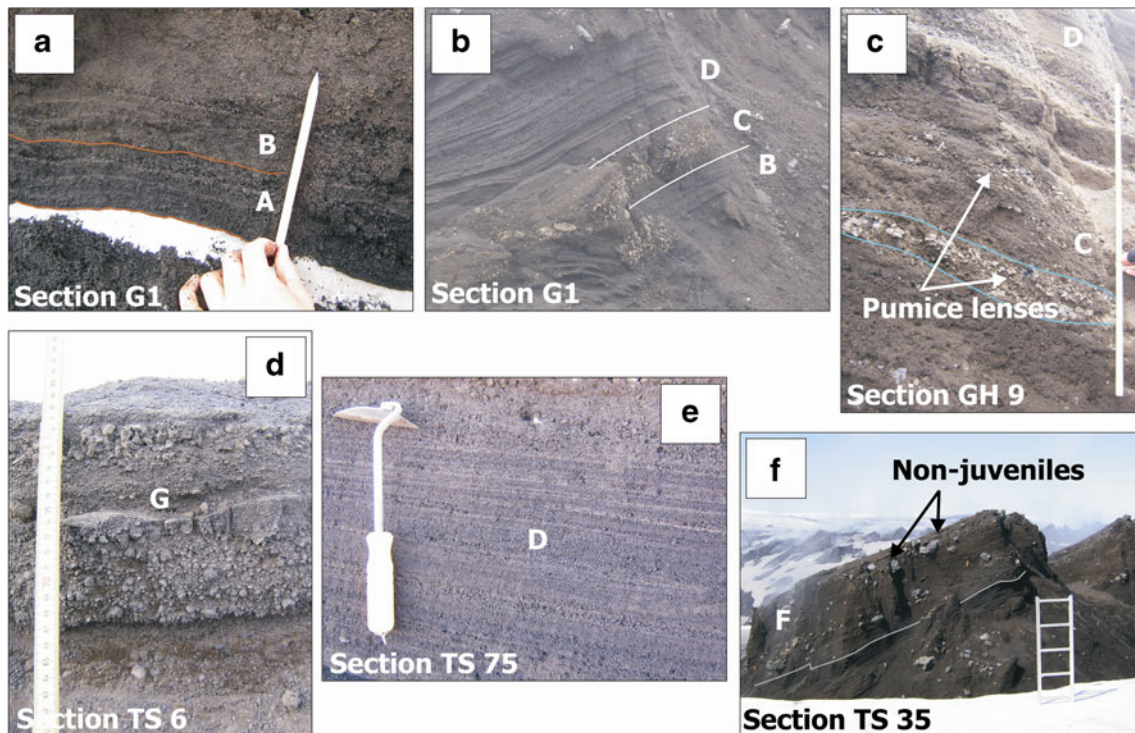
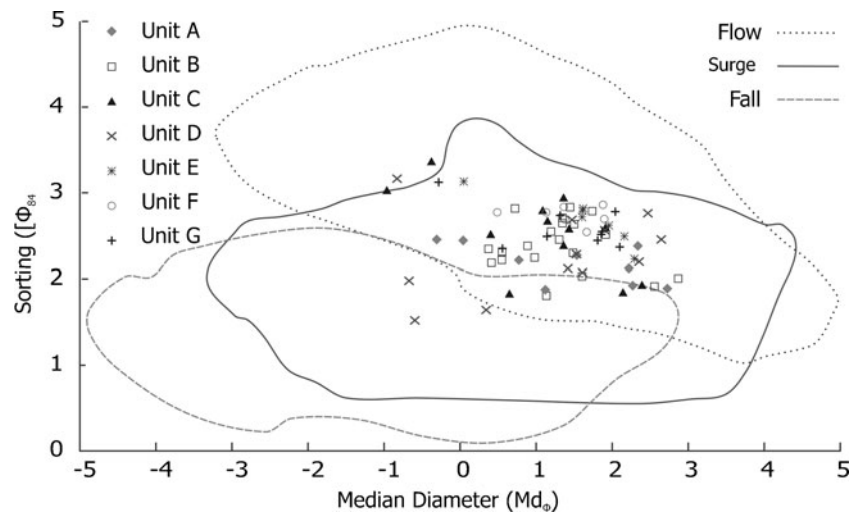


Fig. 10 **a** Units *A* and *B* (boundary between units *A* and *B* marked by brown line). Beds are highlighted by pale brown fine ash. **b** Units *B*, *C*, and *D* (unit *C* is bounded by white lines). At this locality (G1), unit *C* is relatively thin (<60 cm) and is dominated by a pumice-rich bed (pale

brown clasts). **c** Pumice lens within unit *C* (outlined). **d** Unit *G*. **e** Laminae and low-angle crossbeds within unit *D*. **f** Unit *F* (above grey line) containing the abundant coarse non-juvenile fragments

Fig. 11 Plot of median diameter vs. sorting of samples from each unit compared to fields given by Walker and Croasdale (1972)



sorted ($\sigma_{\Phi}=2.7$), but are diffusely layered on a decimetre scale. Certain intervals within the unit exhibit reverse grading and are more distinctly cross-bedded. However, the presence of these intervals is not systematic. Indistinct cross-beds are highlighted by pumice lapilli trains that consist of single-grain-thick (<5 cm), borderline clast/matrix supported layers of sub-angular fine to medium pumice lapilli, which can be traced for >3 m along a section. The crudely layered regions of this deposit lack distinct fine ash partings.

The most distinctive feature of unit C is the presence of numerous lenses (Fig. 10c) which are continuous over tens to hundreds of centimetres and have a maximum thickness of 30 cm. Outstanding features of the lenses are that: (a) they are composed of fines-poor pumice lapilli and bombs within a grain-supported framework, (b) they consist primarily of equant pumice clasts with glassy, commonly cracked, outer surfaces

that are extremely fragile, (c) they have flat bases and truncated tops and sides, suggesting that they have been eroded, (d) they are internally massive or normally graded and (e) the maximum pumice clast size decreases with distance from source. In many cases, pumice lapilli trains are formed in association with (above- or down-current from) the pumice lenses.

The grain size distribution of unit C contains a number of modes (Fig. 9): (1) pumice clasts in the -4Φ to -5Φ fractions, which are largely confined to pumice lenses and trains; (2) moderately vesicular (50–70% vesicularity) clasts in the -2 to -1Φ fractions, which are concentrated in “coarse” cross-bed sets; and (3) a matrix of fine ash ($>2.5\Phi$).

The fine fraction (<1 mm) consists largely of pumice or broken bubble-wall shards (Fig. 13), although it also contains up to 30 vol.% dense (<40% vesicularity) juvenile

Table 3 Average glass compositions (electron microprobe) for single units and a representative melt inclusion

	SiO ₂	TiO ₂	Al ₂ O ₃	FeO	MnO	MgO	CaO	Na ₂ O	K ₂ O	P ₂ O ₅	S (ppm)	Cl (ppm)	% S loss	n
Unit A	50.01	3.00	13.11	14.01	0.24	5.09	9.43	2.90	0.50	0.34	837	182	50	26
Unit B	50.08	3.01	13.06	13.79	0.23	5.09	9.49	2.91	0.51	0.35	831	180	50	72
Unit C	50.00	2.97	13.16	13.73	0.31	5.23	9.62	2.91	0.49	0.33	780	175	53	121
Unit D	50.20	2.93	13.24	13.64	0.23	5.25	9.52	2.96	0.49	0.33	802	181	52	29
Unit E	49.97	2.86	13.21	13.50	0.23	5.41	9.71	2.90	0.48	0.32	818	177	51	69
Unit F	50.05	2.94	13.29	13.62	0.23	5.28	9.62	2.86	0.48	0.32	842	171	50	32
Unit G	49.63	2.96	13.04	13.78	0.23	5.19	9.57	2.90	0.44	0.33	823	174	51	34
Pumice lens	50.27	3.20	12.88	14.35	0.24	4.84	9.28	2.94	0.54	0.35	688	188	59	43
Melt inclusion	48.49	4.22	10.39	19.51	0.29	3.83	7.90	2.53	0.81	0.61	1670	438	–	14

N number of analyses (point analyses of melt inclusions hosted in plagioclase phenocrysts were performed using a Cameca SX100 Electron Microprobe at the University of Edinburgh, UK. This instrument was calibrated against an assortment of natural and synthetic glass and mineral standards. Analyses were conducted using standard WDS technique under the following conditions: accelerating voltage—15 kV; beam current—2 nA for major elements (Si, Al, Fe, Mg, Ca, Na, K) and 80 nA for trace elements (Mn, Ti); beam diameter—5 μm; counting times—20 s for all elements with the exception of Mn and Ti which were 50 and 40 s, respectively. The total time taken for each analysis was approximately 5 min. Analyses of the Lipari and BHVO-2G standards were conducted prior to and at the end of analytical sessions and at regular intervals in between, to mitigate against instrumental drift. ZAF (atomic number, absorption and fluorescence) corrections were applied to the data using XPhi Cameca PeakSight software. For more details on analytical procedure, see Jude-Eton (2011))

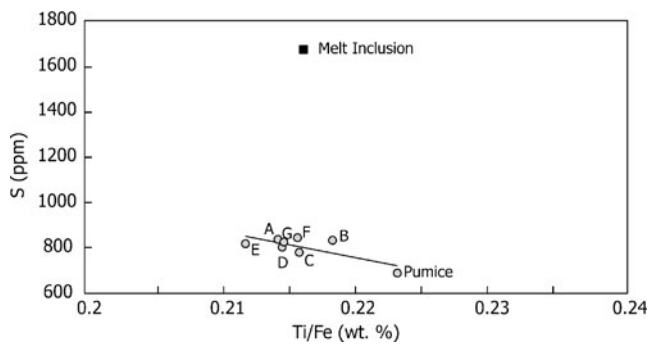


Fig. 12 Average sulphur content of groundmass glass vs. Ti/Fe for each depositional unit (grey circles) via electron microprobe analysis. The maximum value for un-degassed G2004 melt trapped in plagioclase phenocrysts is also shown (black square)

clasts and <1 vol.% of non-juvenile fragments. Again, free crystals are virtually non-existent. Subangular juvenile pumice fragments also make up >90 vol.% of the lapilli fractions, with the remainder consisting of a mixture of non-juvenile and dense juvenile lapilli.

Interpretation

The indistinct bedding and poor sorting of the bulk of unit C suggest deposition from a particle-rich density current of phreatomagmatic origin. By contrast, the internal characteristics (massive to normally-graded, clast supported, fines-poor, lack of clast abrasion) of the pumice lapilli lenses within this unit are consistent with a fall origin. Furthermore, these lenses consist primarily of pumice clasts with glassy, quenched outer surfaces that are extremely delicate, and it is unlikely that such pumice clasts could have survived intact within a turbulent density current. However, the lense morphology (flat bases with truncated tops and sides), along with their context within the deposit indicate syn-depositional erosion. These pumice lapilli lenses are

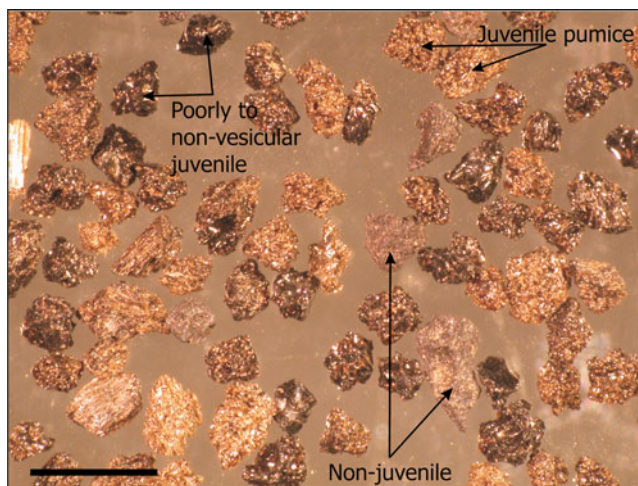


Fig. 13 Tephra grains from unit C of the G2004 deposit

interpreted as remnants of concurrent pumice lapilli fall layers which have been modified by erosion by subsequent PDC. Unit C, as a whole, is therefore interpreted to originate from deposition by hybrid fall and PDC activity. This circumstance is reflected in the unit C (area)^{1/2} vs. thickness relationships (Fig. 8), as a change in thinning rate occur in a region comparable to the observed run-out distance of associated PDC (i.e. 2.5–3 km from source).

Calder et al. (2000) interpreted pumice lapilli-rich layers within the 1993 ignimbrite at Lascar volcano, Chile, as low-density segregations within a concentrated pyroclastic flow, which detached and moved to the margins and distal parts of the flow. This interpretation was supported by reverse grading within pumice lapilli-rich layers and a strong negative correlation between maximum pumice and maximum non-juvenile clast sizes with distance from the vent. However, the pumice lapilli-rich layers within the G2004 deposit are massive or normally graded, maximum pumice clast size decreases with distance from the vent and there is no relationship with the dispersal characteristics of the non-juvenile clasts. These features lend support to our interpretation of the pumice lapilli-rich layers being intercalated fall layers. Similar deposits elsewhere are interpreted to have been generated by hybrid fall and flow processes (e.g. Sohn and Chough 1989; Chough and Sohn 1990; Cole et al. 2001).

The changes in thinning rate within the proximal area can be attributed to variability in run-out distances and dispersal axes of PDC and their variable contribution to the deposit at a given location. Within the medial to distal regions of the deposit, the thinning trend progressively shallows (Fig. 7). The inflection point at 3.5 km for unit C is consistent with the dominant emplacement mechanism changing from PDC to pyroclastic fall at or beyond this distance. We therefore interpret unit C to have been deposited from multiple, closely spaced PDC and contemporaneous intermittent pumice lapilli fallout.

Unit D

Description

Unit D appears to have issued from both vents and was directed principally northwards (Fig. 5). However, as the isopach map shows, it has an irregular outline encompassing two principal lobes that have maximum run-out distances of 3.2 and 2.6 km. Furthermore, the deposit exhibits exaggerated pinch-and-swell morphology which is apparent at the outcrop scale, but not at the scale of the dispersal diagrams (Fig. 8). The unit is confined to the proximal region and $t_{1/2}=290$ m.

Unit D is up to 130 cm thick in the most proximal sections. In most locations where unit D is present, it has a

uniform thickness for the extent of the outcrop. Nevertheless, there are numerous instances where the thickness varies by up to 10 cm within a single section (e.g. section TS60, 360 m northwest of the crater; section TT02B, 550 m north–northwest of the crater; section TS80, 1,100 m north of the crater).

This unit is pale to dark brown and consists of many (20 on average) alternating very fine ash and fine lapilli laminae and very thin beds that exhibit very low angle cross beds (Fig. 10e). Separate packets are draped by very fine pale brown ash. The unit is reverse-graded overall.

The grain size distribution of unit D is polymodal. Modes occur at 0.5Φ , 2.75Φ and 3.75Φ . Well sorted, fines-poor packages consist of -0.5 to 0.5Φ , sub-rounded scoria. The finer beds are relatively poorly sorted and >90 vol.% of grains are $>0\Phi$ in diameter. Finer beds contain larger proportions of poorly vesicular fragments, and have average contents of ~ 90 vol.% scoria, ~ 5 vol.% non-vesicular juvenile glass and ~ 2 vol.% juvenile bubble-wall shards.

Interpretation

The internal characteristics, thickness variations and spatial distribution of unit D are consistent with deposition from a number of dilute, localised PDC generated by phreatomagmatic activity. This interpretation is also demonstrated by the fine-scale features of this layer. For example, in section TT02B, unit D varies in thickness between 33 and 41 cm along a 10-m-long transect and in places, internally cross-bedded lenses can be observed to pinch out and overlap one another, separated by 10–20 cm of unstructured fine ash and medium pumice lapilli. In section TS60, a 5–8 cm thick, faintly cross-bedded layer is overlain by 3–7 cm of massive medium to fine ash. Distinct coarse layers are draped by ash. In section TS80, the thickness of unit D varies by up to 3–4 cm along a 5-m-long transect. The observed thickness variations within unit D are primary and cannot be a response to substrate topography because tephra was deposited on an essentially flat surface. Undulation of the ice contacts are not evident in any section nor are the contacts between unit D and underlying layers irregular. The thickness variations evident in this unit are therefore a consequence of emplacement by PDC.

The spatial distribution of unit D is not consistent in every region of the G2004 deposit. This layer was not deposited in some areas, whereas in others it is unexpectedly thin or thick (Fig. 14). The distinctive fine ash layers draping each cross-bed set indicate more prolonged time intervals between PDC than in unit C. However, the time available for settling of fine ash above single PDC layers could equally have been extended by the erratic dispersal, because successive PDC layers were not necessarily emplaced directly on top of one another.

Unit E

Description

The geometry of the unit E isopachs (Fig. 6) demonstrates that it issued from the western vent and was directed northwards. It is dominantly confined to the western regions of the study area. The geometry of unit E is similar to and overlaps that of unit C, but has a more narrowly confined lateral extent. Due to their similarity in nature and the lack of a distinct contact, in many sections in this region it is virtually impossible to determine the boundary between units C and E if the unit D marker layer is not present.

Unit E has a maximum thickness of 2.65 m in the most proximal section of the western dispersal area (Fig. 14). On a semi-log plot of $(\text{area})^{1/2}$ vs. thickness (Fig. 8), this unit shows a stepwise, decreasing trend consisting of four segments, similar to unit C. There is an inflection point in the thinning profile for unit E at 2 km from source. At this point, the average $t_{1/2}$ value changes from 190 m to 6 km.

The bedding characteristics of unit E are virtually identical to those of unit C, differing only in the following: (1) pumice lapilli lenses (*sensu stricto*) are sporadic in unit E, whereas they are abundant in unit C; in unit E, pumice lapilli trains are more abundant; (2) unit E contains a higher proportion of coarse, angular, dense, basaltic non-juvenile fragments. These clasts are concentrated in specific layers or among pumice lapilli trains.

The top 100–150 cm of unit E consists of numerous diffusely layered intervals, intercalated with pumice lapilli lenses and trains. Pumice lapilli lenses are up to 10 cm thick and can be traced for more than 3 m in sections oriented along the dispersal axis. Such lenses may appear like tabular layers, but taper towards the edges in long exposures. In the bottom part of the unit, pumice lapilli lenses are uncommon. Instead, layers are defined by a number of rather diffuse pumice lapilli trains. Layered intervals tend to fine upwards, although the unit is quite poorly sorted overall ($\sigma_{\Phi}=2.7$).

The unit E pumice lapilli lenses generally consist of equant pumice clasts (60–80% vesicularity) with quenched rinds, which are dominantly in the medium to coarse lapilli size interval but range up to 10 cm in diameter. In contrast, the trains consist of fragments of such pumice clasts, which are sub-angular and do not have continuous quenched surfaces. Abundant, 5–10 cm, orange to red, non-juvenile fragments also occur within pumice lenses. Although the lenses have the overall appearance of being clast-supported, pumice and non-juvenile clasts are fine ash-coated. The unit E matrix dominantly comprises fine ash, although grains range from -0.5 to 4Φ in diameter and $Md_{\Phi}=0.75$. Unit E components are similar to those of unit C, but there is a higher proportion (up to 80 vol.%) of fragments with 50–80%

vesicularity. In the finer size fractions (-2Φ and smaller), there are fewer than 2% non-juvenile clasts.

Interpretation

The characteristics of unit E are almost identical to those of unit C. Together, these two units make up about 80% of the mass of the subaerial G2004 deposit and represent the main phase of eruptive activity, which was dominantly phreatomagmatic. The two units were both produced by fallout from the eruption column concurrently with PDC. A change in thinning rate coincides with the run-out distance of associated PDC. Consequently, the dominant emplacement mechanism for unit E changes from PDC to pyroclastic fall between 2.5 and 3.5 km from source.

Key differences between units E and C, such as the relative abundance of non-juvenile fragments, the predominance of pumice trains over pumice lenses and the slight differences in dispersal characteristics (particularly $t_{1/2}$ values) suggest that at this time (1) there was less time between successive PDC than earlier in the eruption and/or (2) a greater proportion of the unit was emplaced via PDC (as compared to fall) than previously.

Unit F

Description

The maximum extent of unit F is 2.5 km from the source. The layer is therefore confined exclusively to the proximal area and dominates the small eastern lobe of the G2004 deposit. Unit F is dispersed within a sector trending from east to north–northeast, quite unlike the other units from this event. However, the isopachs cannot be used to distinguish the source vent for this layer as the innermost mapped isopach line encompasses both the eastern and western eruption centres.

Section TT01 (located approximately 550 m north–north-east of the centre of the 2004 crater) is the only location at which all identified units are present together (Fig. 9). At this location, unit F overlies unit E. Unit F has a maximum thickness of 2.5 m in the most proximal section of the eastern dispersal area and exhibits a very steep, but uniformly linear thinning geometry ($t_{1/2}=190$ m). There is a clear inflection in the thinning trend for unit F between 500 and 700 m from the vent, beyond which the unit follows a simple pattern of exponential decay (Fig. 8).

Unit F is grey–brown, massive and very poorly sorted. Impact sag structures are commonly present below the larger non-juvenile clasts, identifying them as ballistically emplaced clasts. The grain size distribution is polymodal; dominant modes occur between -2 and 4Φ and, apart from

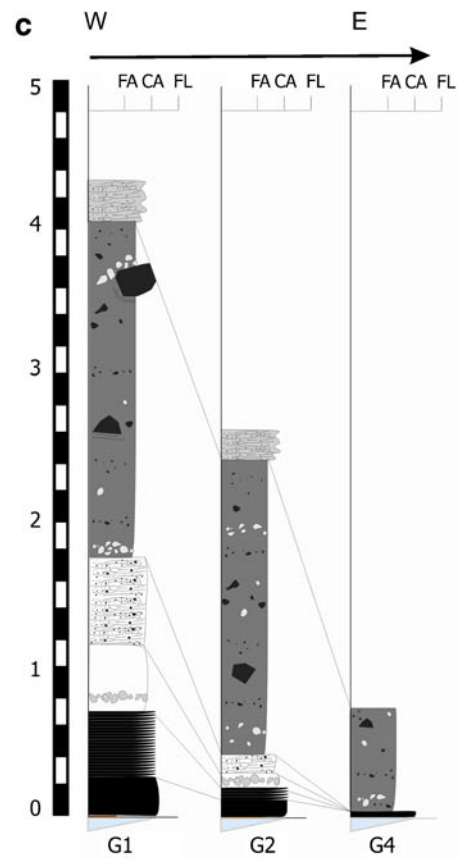
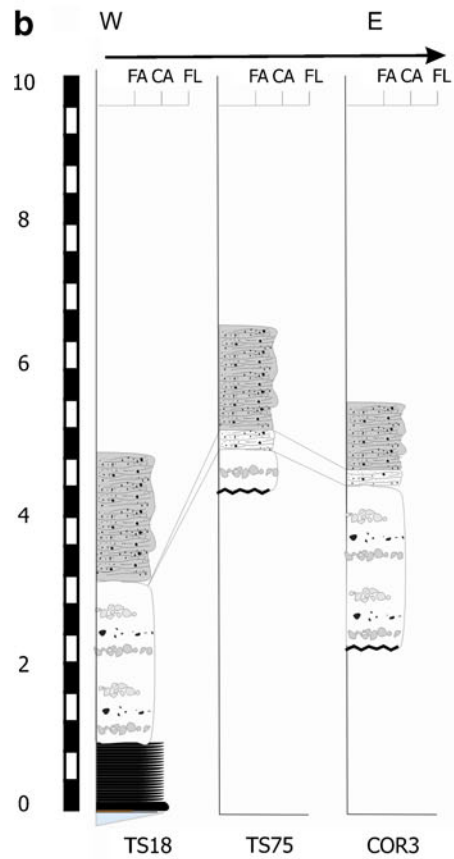
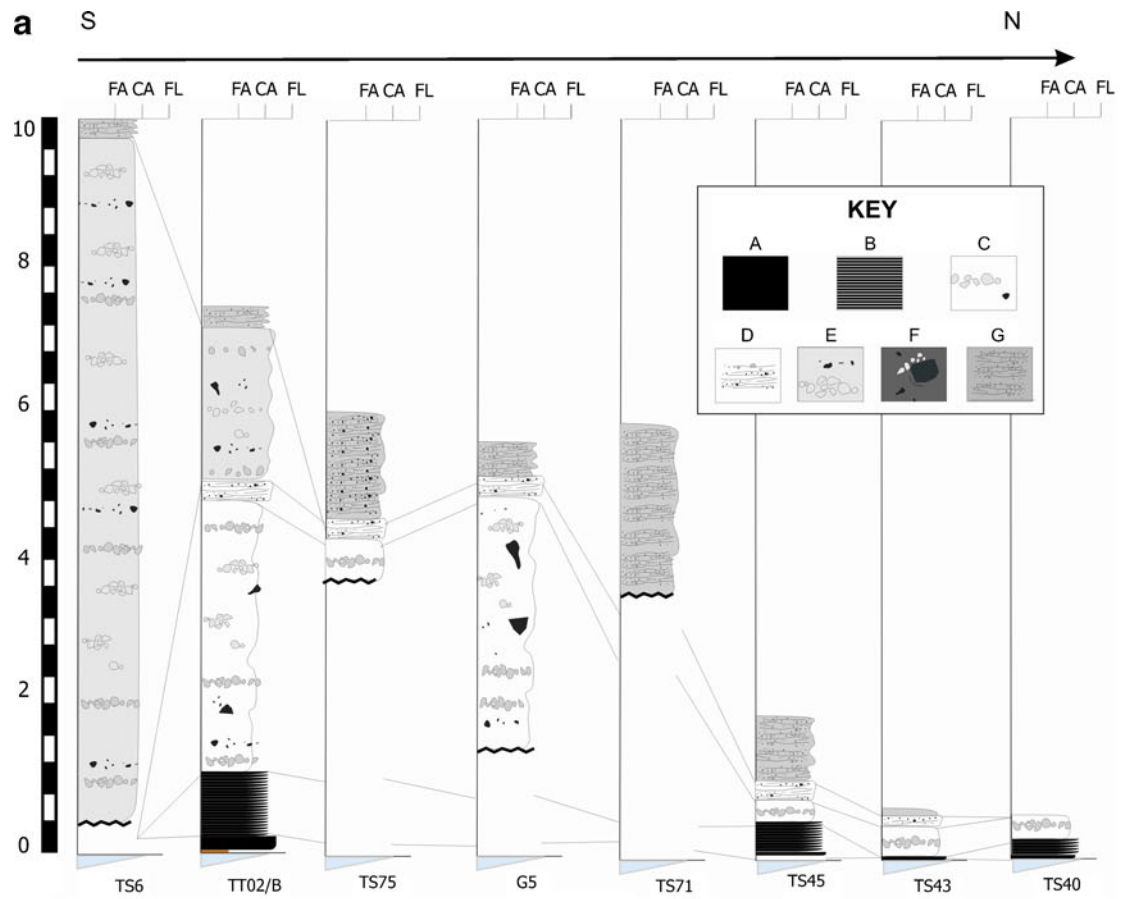
Fig. 14 Correlation of stratigraphy. **a** A transect along the principal direction of dispersal (S–N). **b** A transect from W to E in the far western part of the 2 deposit. **c** A transect from W to E in the far eastern part of the deposit. FA fine ash, CA coarse ash, FL fine lapilli, CL coarse lapilli

outsize non-juvenile clasts in the top half of the layer, do not vary with stratigraphic height. Fine ash dominates; 70 wt.% of samples fall into size fractions $<1\Phi$. The fine to medium lapilli size fractions consist predominantly of pumice clasts (>80 vol.%) in the lower part of the unit. In the upper part, this size fraction is dominated by non-juvenile clasts (up to 60 vol.%). The finer size classes consist of roughly equal proportions of scoria and pumice. The -1 to -2Φ size fractions contain <5 vol.% non-juvenile fragments and these are not present at all in size classes finer than -1Φ .

Interpretation

Unit F is massive and very poorly sorted, and has limited and directed dispersal along with a relatively high abundance of non-juvenile fragments compared to the rest of the deposit. The grain size distribution does not vary within the layer, but the very poor sorting and high abundance of fine ash reflect its phreatomagmatic origin.

The stratigraphic sequence observed at section TT01 clearly demonstrates that unit F is the product of a distinct event that occurred some time after, and independently of, the deposition of unit E, rather than occurring at the end of the C-phase of activity or as a minor episode during the E-phase. On the morning of November 3, a spike in tremor amplitude occurred (Fig. 3). Close to this time, the plume dropped below radar detection limits. We postulate that the eruption column lost buoyancy and collapsed, resulting in deposition from a single, directed, high concentration PDC. The current was directed towards the east to east–northeast and unit F was deposited in the eastern dispersal area only. Unit E is only present in the western part of the dispersal area because it was issued from the western vent and has a narrowly confined lateral extent due to the action of a strong southerly wind at this time during the eruption. In contrast, unit F is only present in the very eastern part of the dispersal area because it represents a directed column collapse event and unlike all the other units, which were dispersed northwards, it was directed towards the east. It is not clear from the dispersal patterns which of the two vents produced unit F. However, the eruption column that produced unit E was focussed on the western vent so it is likely that the unit F products also came from the western vent. There is a notable abundance of non-juvenile blocks within unit F. The presence of impact sags underlying many of these clasts indicates ballistic emplacement (i.e. not part of the eruption column collapse). It is therefore possible that the ballistic blocks were ejected from the eastern vent prior to the deposition of unit G.



Unit G

Description

Unit G isopachs are rather broad, enclosing much of the ice cauldron. Hence, the source vent is not clear from this geometry (Fig. 6). However, visual observations indicate that only the eastern vent remained active towards the end of the eruption.

Unit G consists of two distinctive lobes, each of which has a low aspect ratio. Unit G is dominant in the west, but extends to a few of the most proximal sections in the east. The unit is largely confined to the proximal area and dies out within 3 km of the vent along the principal dispersal axis (Fig. 7). Unit G ranges from 20 to 50 cm in total thickness and exhibits a relatively shallow thinning rate ($t_{1/2}=400$ m).

Unit G consists of one to three, grey–brown sub-units that exhibit low-angle cross-beds. In general, cross-bed sets are reversely graded. However, although diffusely layered, the deposit is not well ordered, as coarse grains are not confined to dominantly coarse bed sets. This unit is poorly sorted, and notably fines rich (over 75 wt.% <1 mm in diameter), even very close to the vent. The remainder consists of very coarse ash to fine lapilli. The fine lapilli consist of grey, angular non-juvenile clasts and juvenile pumice clasts in modal ratios ranging from 1:1 to 1:2. Fine lapilli are concentrated in pumice-rich layers towards the top of bed sets. Clasts coated with fine ash are common in the fine lapilli size fraction, whereas rare “rim-type” accretionary lapilli (Schumacher and Schmincke 1995; Fig. 15a) and more common armoured clasts (Waters and Fisher 1971; Fig. 15b) are present in the most proximal unit G. Scattered non-juvenile blocks 5–20 cm in diameter are also present in this layer. The coarse ash to very coarse ash consists of juvenile scoria and pumice in a 3:2 ratio. In contrast, the fine ash fraction consists almost entirely of glass shards derived from the disintegration of highly vesicular (>80% vesicles) pumice.

Interpretation

The poorly sorted nature of unit G, along with the presence of abundant non-juvenile fragments and ash-coated clasts, are diagnostic of phreatomagmatic PDC deposits. The diffuse cross-stratification reflects relatively low particle concentrations within the current. The presence of armoured clasts and accretionary lapilli indicates that 10–15 wt.% liquid water was present in the eruption column (Gilbert and Lane 1994; Schumacher and Schmincke 1995).

Event reconstruction

It is reasonable to expect that large changes in eruption behaviour or vent conditions are reflected in changes in the tremor

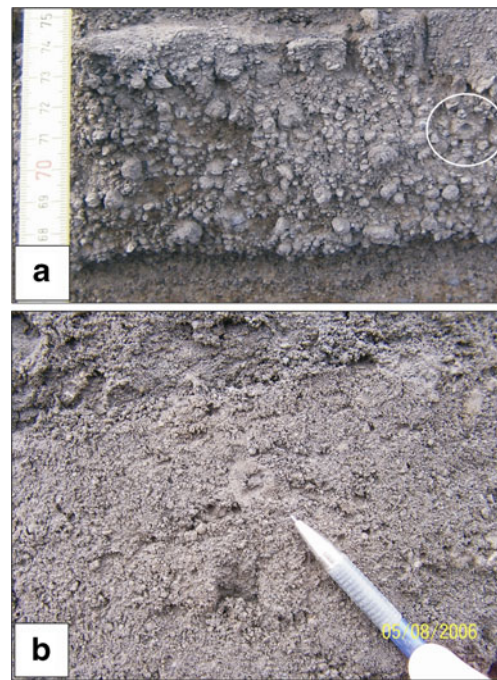


Fig. 15 **a** Unit G at section TS50 contains abundant coated clasts (white circle, a hole left in the deposit where a lapillus has been plucked out and the coating has been preserved). **b** Rim-type accretionary lapillus in unit C from section TT02

signal which is the only record of the eruption with no gaps in data. Although tentative, spikes and sudden changes in tremor are here correlated with the onset of formation of single units, using the plume record as an additional constraint (Table 4).

The onset of tremor at 21:50 on November 1 corresponds to the onset of the subglacial eruption (Fig. 16, panel 1). The subglacial phase of the eruption lasted for at least 23 min, during which time it melted through the 150–200 m thick ice cover to the surface. The juvenile clasts in unit A and B suggest that the magma in the initial subaerial phase was largely outgassed before fragmentation, indicating that a portion of the magmatic volatiles had decoupled from the melt as it rose through the conduit. The escape of magmatic gases may have initiated ice melting, which eventually led to the formation of a subglacial cavity and supplied water for the onset of phreatomagmatic fragmentation during the first subaerial phase of the eruption.

The initial tremor spike at 22:13 is thought to signal the end of a fully subglacial eruption and the onset of the first subaerial phase, which we think lasted for over 3 h and included the deposition of units A and B. The eruption plume was first detected by weather radar 37 min later at 22:50 (Fig. 3). The first subaerial phase of G2004 produced a proximal phreatomagmatic fall layer (unit A; Fig. 16, panel 2). Unit A was directly followed by emplacement of PDC (unit B), which have a maximum thickness of 80 cm and attain maximum run-out distances of 3–3.5 km. Together, units A and B (subaerial phase 1) account for <15 wt.% of the

Table 4 A summary of the timing of onset, duration, and termination of each unit, based on time series analysis of plume height, tremor amplitude, and photographs of the eruption

Unit/phase	Start time	End time	Duration (h)	Cauldron (m ³ /s)	Proximal (m ³ /s)	Distal (m ³ /s)	Total (m ³ /s)
Subglacial	1 Nov. 21:50	1 Nov 22:13	0.4	150	0	0	150
A+B	1 Nov. 22:13	2 Nov 01:27	3.2	141	77	0	218
C	2 Nov. 01:27	2 Nov. 19:32	18.1	98	51	32	181
D	2 Nov. 19:32	2 Nov. 21:03	1.9	57	57	0	114
E	2 Nov. 21:03	3 Nov. 09:58	12.9	27	35	32	93
F	3 Nov. 09:58	3 Nov. 11:21	1.4	0	46	0	46
G	3 Nov. 11:21	3 Nov. ~18:15	6.9	0	19	0	19

total erupted magma volume. They were formed by a short-lived explosive event generated by the interaction of partly degassed magma and glacial meltwater. The deposition order clearly suggests fallout from a plume of moderate height above the eastern vent, followed by PDC emplacement produced by column collapse towards the end of this eruption phase (Fig. 16, panel 3). At the end of subaerial phase 1, there

was a momentary lull in the tremor amplitude, after which it rapidly intensified to an oscillating steady state level. The next phase of the G2004 eruption is considered to be the main phase of activity and produced units C, D, E and F (subaerial phase 2).

The period of unit C deposition is taken to correspond to a period of less-elevated and continuous tremor from 01:27

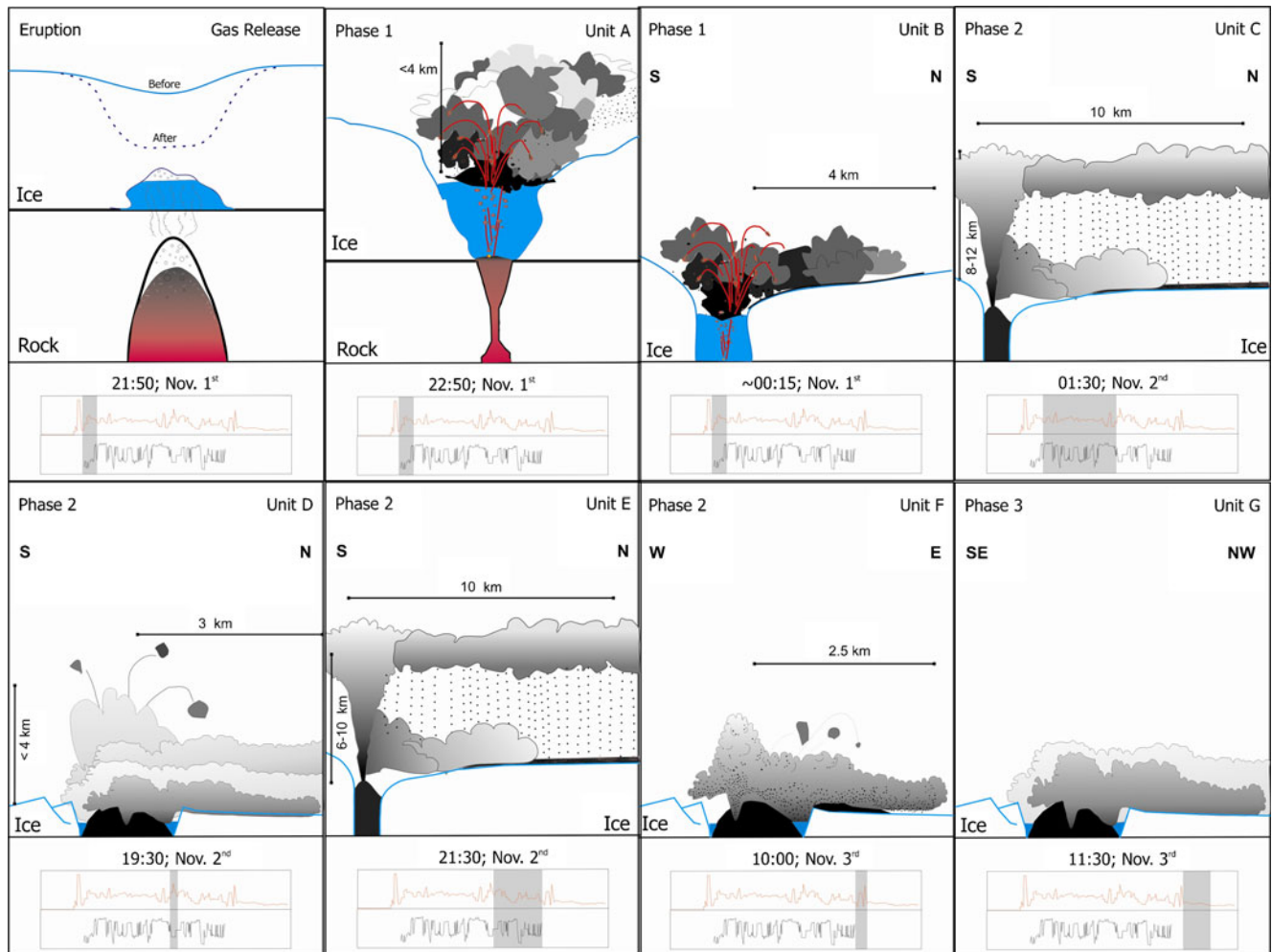


Fig. 16 Schematic diagram depicting the G2004 eruptive events and depositional units. *White* represent ice, *blue* water, *red* magma, *black* tephra. Note that this cartoon representation is not to scale

to 19:32 on November 2 (Fig. 3). This inference is consistent with the sustained activity indicated by visual observations. Unit C forms ~50% of the total subaerial deposit volume and the observation of two vigorously active vents is consistent with unit C isopach geometry (Fig. 6). Tephra was deposited by coeval fall and PDC mechanisms (Fig. 2a, b, and f). Continuous uprush activity dominated, although both visual observations and tremor records show this activity was punctuated by occasional, higher energy pulses. Photographs taken on the late afternoon of November 2 (Fig. 2) show that the western vent became dominant towards the end of unit C deposition and the plume became increasingly steam rich (Fig. 16, panel 4).

The tremor spike which occurred at 19:32 on November 2 is thought to correspond to the onset of unit D deposition. The eruption intensity abruptly diminished and there was no significant pause between this and the previous activity. Unit D deposition therefore lasted for 3 h. During this period, the plume stepped down and disappeared below radar detection for 63 min (Fig. 3). Unit D consists of laminated and distinctly cross-bedded PDC deposits of limited lateral dispersal within the northeastern sector of the tephra blanket, consistent with sedimentation from very dilute currents (Fig. 16, panel 5). A rhythmically oscillating tremor phase ensued before the plume rose again with the onset of unit E at 21:30 h. With the eruption column re-established, a similar style of activity to that of unit C resumed but was focused on the western vent and therefore unit E only occurs in a relatively narrow band towards the western half of the deposit (Fig. 15). Unit E deposition lasted for 12 h and 55 min during which time the combined processes of pyroclastic fall and PDC emplacement operated (Fig. 16, Panel 6). This period of rapidly oscillating, sustained activity culminated in a spike in tremor intensity at 09:58 on November 3, lasting for only 1 h and 23 min, which we correlate to the eruption of unit F. One possible scenario is that sudden loading of the column corresponding to a short-lived pulse of high magma discharge caused it to lose buoyancy and collapse towards the east resulting in the deposition of unit F (Fig. 11). An equally plausible scenario is that the eruption of unit F corresponded to a vent-widening event, which is consistent with the high non-juvenile clast content.

Emplacement of unit F was the last event of the main phase of the eruption (Fig. 16, panel 7). After this, the eruption column was never fully re-established and tremor amplitude plummeted to a low level. The duration of the final part of deposition towards the north is difficult to determine but we propose that it had come to an end by 18:16 on November 3, when the tremor amplitude dropped to background levels. The stratigraphy indicates that the final activity on November 3 resulted in the emplacement of two PDC beds north and northeast of the vent (unit G; Fig. 16, panel 8). During November 4, the plume rose 1–2 km above the vent. Aerial inspections on November 5

revealed no additional deposits outside of the ice cauldron. The eruption may have ceased on November 5, but tremor continued to be recorded until November 6 and the end of the eruption has been set at this date (Vogfjörð et al. 2005; Sigmundsson and Guðmundsson 2004).

Time breaks during the Grímsvötn eruption

The IMO plume height data along with visual observations of the plume on November 3 indicate that there were no breaks in discharge from the vent over the course of the G2004 eruption. Furthermore, the continuous tremor record strongly suggests that there were no significant pauses in magma emission. The proximal 2004 succession contains several intercalated PDC deposits (Figs. 8, 16), all of which are either absent, or represented only by coeval ash fall, in medial and distal sections. The majority of these PDC are sector-confined and the accompanying variability in proximal fall dispersal (resulting from vent migration and changing wind directions) means that these distinct PDC beds are not firm indicators of significant time breaks in ash fall. Deposition during the G2004 event is therefore considered to have been continuous overall.

Magma discharge

The main part of the G2004 eruption lasted for 45–46 h (subglacial+units A–G), beginning at 21:50 on November 1. Average discharge rates for single eruption units, based on unit volume (Table 1) and calculated filling rate of the ice cauldron (Fig. 4) are presented in Table 4 and Fig. 17.

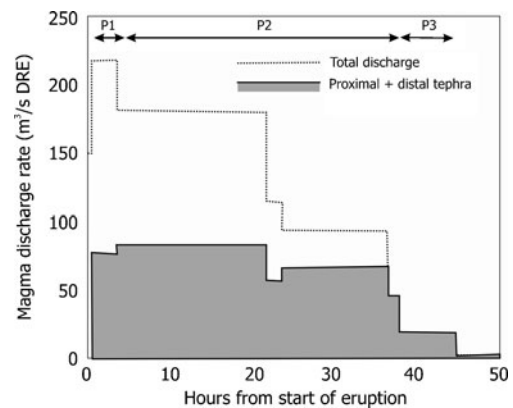


Fig. 17 Average discharge over time throughout the G2004 eruption, based on unit mass and the calculated filling rate of the ice cauldron. The proportion of mass contributed to the subaerial deposit beyond the limits of the ice cauldron is shaded in grey. Filling of the cauldron dominated the discharge to start. During deposition of unit D, plume-transported discharge equaled the filling of the cauldron. The designations P1, P2 and P3 correspond to the duration of the three subaerial eruption phases

Filling of the cauldron dominated the discharge at the beginning; only during deposition of unit D did plume-transported discharge equal the contribution to filling the cauldron. Average mass discharge rates of each unit are broadly consistent with their respective average and maximum tremor amplitudes. The subaerial phase 1 units (A and B) are considered together as they were generated by a continuous phreatomagmatic event and cannot be distinguished from one another on the tremor or the plume records. This first phase of activity was the most intense; the calculated discharge rate was $218 \text{ m}^3 \text{ s}^{-1}$ and peak tremor amplitude was $8 \mu\text{m s}^{-1}$. The average discharge rate during unit C deposition was somewhat lower ($181 \text{ m}^3 \text{ s}^{-1}$), although the observed oscillations in plume height and possibly also fluctuations in tremor amplitude are consistent with temporal instabilities in the column. Unit D deposition is marked by a decline in magma discharge rate ($114 \text{ m}^3 \text{ s}^{-1}$) compared with that of unit C. Column collapse at this time could have been associated with an influx of water into the vent (i.e. magmatic heat would be transferred to the water rather than the eruption column), or with a pressure drop in the conduit associated with vent migration. Up to this stage, both vents were simultaneously active. The eruption column was re-established on the western vent at the onset of unit E deposition. The average magma discharge rate during this time was $93 \text{ m}^3 \text{ s}^{-1}$. Overall, the average magma discharge rate declined with time during the G2004 eruption.

During unit C sedimentation, the median tremor amplitude was closer to $6 \mu\text{m s}^{-1}$ and during formation of unit D, it reached $11 \mu\text{m s}^{-1}$. During deposition of unit E, it oscillated around $4 \mu\text{m s}^{-1}$. The total rate of magma discharge during unit C deposition was twice that of unit E, yet the dispersal trends, style of activity and nature of deposits are remarkably similar. Using the mass deposited on the glacier surface (tephra apron) outside the ice cauldron gives an apparent magma discharge of $83 \text{ m}^3 \text{ s}^{-1}$ for unit C and $67 \text{ m}^3 \text{ s}^{-1}$ for unit E. Here, the difference in discharge rate and therefore in the amount of energy supplied to the plume by the two eruption periods is less pronounced. Plume height records show that the unit C plume was slightly higher and more stable column than that of unit E and the stratigraphic record concurs that unit C contained a larger component of emplacement by tephra fallout. The higher overall $t_{1/2}$ values of unit C, particularly within the proximal region of deposition, are also consistent with this assessment. In this case, the comparison of “apparent discharge” between the two units is instructive because although the actual magma discharge rate during unit C was much greater, most of the products were confined to the ice cauldron and not dispersed supraglacially. Only a portion of the magma and its thermal energy was expended on the plume. Therefore, despite the considerably higher magma discharge rate during unit C, the supraglacial deposit characteristics

are similar to those of the less energetic unit E. The dispersal characteristics of units C and E may have been controlled by differences in eruption column dynamics rather than by changes in the rate of magma supply.

The abrupt increase in tremor amplitude ($11 \mu\text{m s}^{-1}$) associated with the onset of unit F deposition is consistent with the interpretation of a vent-clearing event at the beginning of this eruption unit, as suggested by the non-juvenile-rich componentry. A short-lived eruption column then collapsed, accounting for the bulk of unit F deposition. Discharge continued to wane for the remainder of the eruption and a sizable eruption column was never re-established. We have calculated a discharge of $19 \text{ m}^3 \text{ s}^{-1}$ for unit G, but this value is uncertain because of the poor constraints on the absolute end time for the unit. At this stage, the eruption was waning, generating relatively low-intensity PDC.

Sectoral patterns of distribution

The most prominent feature of the G2004 total thickness isopach map (Oddsson 2007) is that the deposit is bi-lobate. We infer that in the proximal area, vent migration and sectoral patterns of PDC distribution account for this geometry. However, the extension of these lobes into the distal region of the deposit can only be controlled by changes in wind direction.

Proximal fall and PDC layers show varying degrees of confinement to sectors around the vents. This pattern is manifest in the lobate distribution patterns of PDC units B, D and G, in the directed nature of unit F, and in the relatively narrow distribution of the late fall unit, E (Fig. 6). The dispersal axes of fall-dominated units (C and E) appear to be controlled by the strong regional wind acting throughout the eruption, whereas the PDC lobes are also distributed according to additional geometric factors such as the vent of origin and asymmetric column collapse. PDC dispersal was also controlled by the presence of the 300-m-high caldera wall directly to the south of the vents.

Factors affecting dispersal of the G2004 tephra

Semi-log plots of $\text{area}^{1/2}$ vs. thickness (Pyle 1989) are used to evaluate and compare key characteristics of plume-generated tephra fall deposits (Fig. 8). However, equivalent models do not yet exist for deposits from small basaltic phreatomagmatic eruptions, in which the relationships among magma discharge, plume height and thinning trends are affected considerably by the presence of water in the plume and by deposition from PDC. Two principal factors account for the deviation of the G2004 overall dispersal trend from that of the equivalent “dry” eruption: (1) short-

term eruption column instability resulting in abrupt transitions between deposition by fall, PDC and hybrid processes and (2) the abundance of fine ash in the proximal deposits.

The dispersal diagram constructed using total deposit thickness values for G2004 (Fig. 9), most closely fits a power law trend, but may also be considered to display segmented exponential thinning. Consequently, the deposit, as a whole, “looks” very much like a fall deposit. However, minor proximal and local over-thickening is apparent due to the presence of intercalated PDC deposits (i.e. units B, D, F and G), which exhibit linear thinning relationships within the proximal region of deposition (Figs. 7, 8). This result is consistent with our observation that PDC deposits account for less than 30% of the mass of the tephra apron. It also reveals that the main phase units (units C and E), for which there is clear field evidence for concurrent deposition by fall and PDC, are dominated by a fall signature.

Most layers of the G2004 deposit contain between 60 and 80 wt.% ash less than 1 mm in diameter. Principal modes are usually in the 1 to -1Φ range and secondary modes occur at 3–4 Φ (Fig. 9). Particle aggregation resulting in enhanced proximal deposition of ash is common in a wet plume environment (e.g. Gilbert and Lane 1994). The influence of particle aggregation and the premature deposition of fine ash in the G2004 deposit is evident from the predominance of fine ash in proximal sections and the presence of coated clasts (unit E) and accretionary lapilli (units E and G) in both fall and PDC deposits. An additional factor that is particularly pertinent to eruptions within a glacial environment is the scavenging of fine ash by atmospheric precipitation (e.g. Rose et al. 2008). G2004 took place in the winter and it snowed for part of the eruption.

Subglacial emergent vs. conventional phreatomagmatic eruptions

In terms of deposit characteristics and eruption styles, the G2004 eruption was similar to other basaltic phreatomagmatic eruptions. The differences lie in the relationship between magma discharge and plume height and tephra dispersal. During the early part of the eruption, the majority of the magmatic heat energy was apparently used to melt ice and to deposit tephra in the ice cauldron. The eruption followed the common pattern of basaltic eruptions from a single magma source in which high initial magma discharge is followed by a gradual decline. However, as the eruption progressed, ice melting declined, making a proportionally higher fraction of the magmatic heat energy available for plume generation. As a consequence, establishment of the plume was delayed and was significantly subdued relative to the total magma discharge rate for the first 15–20 h. This effect diminished in the latter part of the eruption, during

deposition of unit E. Hence, a plume of similar size was maintained for some 30 h despite a large drop in magma discharge rate over this period.

Conclusions

The supraglacial deposit of the G2004 eruption was generated by the subaerial phases of a small-volume, basaltic, subglacial eruption. Such sequences are seldom, if ever, preserved in the geologic record because of the nature of their setting. The style of activity and resulting deposits most closely resemble those of emergent Surtseyan eruptions (Thorarinsson 1964; Sohn and Chough 1992; Smellie and Hole 1997; Cole et al. 2001). G2004 was characterised by phases of continuous uprush during which a highly unstable 6–10 km high plume produced widely dispersed, pumice-rich, tephra fall at the same time as generating locally dispersed PDC. Tephra fall was interrupted by total column collapse events marked by the emission of PDC containing a high proportion of fine ash. Although rooster tail jets were observed during the G2004 event, there is no evidence to suggest that this eruption style formed a significant component of the proximal deposit. Correlation of the seismic tremor, plume height and visual observation records show that the rate of magma discharge gradually declined over the course of the eruption, apart from when continuous uprush was punctuated by column collapse events which represent spikes in eruption intensity. Overall, the G2004 deposit is remarkably similar to that of a dry tephra fall deposit on a plot of thickness vs. (area)^{1/2} in that the thickness fits either a power law or segmented exponential thinning trend. Nevertheless, the trend deviates in the proximal area due to the presence of PDC units which are best described by linear thinning trends.

Acknowledgments The authors gratefully acknowledge the support of the following agencies and individuals, without the help of whom this work would not have been possible: A RANNÍS grant covered analytical and fieldwork costs; TC Jude-Eton received a Rannsóknánámssjóður studentship and another from the University of Edinburgh; JÖRFÍ (the Icelandic Glaciological Society) provided equipment, expertise and assistance in the field. The manuscript was vastly improved by the insightful reviews of Ármann Höskuldsson, Jocelyn McPhie and Ian Skilling.

References

- Albino F, Pinel V, Sigmundsson F (2010) Influence of surface load variations on eruption likelihood: application to two Icelandic subglacial volcanoes, Grímsvötn and Katla. *Geophys J Int* 181:1510–1524
- Alfaro R, Branðsdóttir B, Rowlands DP, White RS, Guðmundsson MT (2007) Structure of the Grímsvötn central volcano under the Vatnajökull icecap, Iceland. *Geophys J Int* 168:863–876

- Björnsson H (1988) Hydrology of ice caps in volcanic regions. *Soc Sci Isl* 45:139
- Björnsson H (2003) Subglacial lakes and jökulhlaups in Iceland. *Glob Planet Chang* 35:255–271
- Björnsson H, Guðmundsson MT (1993) Variations in the thermal output of the subglacial Grímsvötn caldera, Iceland. *Geophys Res Lett* 20:2127–2130
- Calder E, Sparks RSJ, Gardeweg MC (2000) Erosion, transport and segregation of pumice and lithic clasts in pyroclastic flows inferred from ignimbrite at Lascar Volcano, Chile. *J Volcanol Geotherm Res* 104:201–235
- Carey S, Sparks RSJ (1986) Quantitative models of the fallout and dispersal of tephra from volcanic eruption columns. *Bull Volcanol* 48:109–125
- Chough S, Sohn YK (1990) Depositional mechanics and sequences of base surges, Songaksan tuff ring, Cheju Island, Korea. *Sedimentology* 37:1115–1136
- Cole PD, Guest JE, Duncan AM, Pacheco JM (2001) Capelinhos 1957–1958, Faial, Azores: deposits formed by an emergent surtseyan eruption. *Bull Volcanol* 63:204–220
- Davies SM, Larsen G, Wastegård S, Turney CSM, Hall VA, Coyle L, Thordarson T (2010) Widespread dispersal of Icelandic tephra: how does the Eyjafjöll eruption of 2010 compare to past Icelandic events? *J Quat Sci* 25(5):605–611
- Fierstein J, Nathenson M (1992) Another look at the calculation of fallout tephra volumes. *Bull Volcanol* 67:350–357
- Folk RL, Ward WC (1957) Brazos River bar [Texas]; a study in the significance of grain size parameters. *J Sediment Res* 27(1):3–26
- Gilbert JS, Lane SJ (1994) The origin of accretionary lapilli. *Bull Volcanol* 56:398–411
- Guðmundsson MT (1989) The Grímsvötn caldera, Vatnajökull: subglacial topography and structure of caldera infill. *Jökull* 39:1–20
- Guðmundsson MT (2005) Subglacial volcanic activity in Iceland. In: Caseldine C, Russell A, Harðardóttir J, Knudsen O (eds) *Iceland—modern processes and past environments*. Elsevier, New York, p 420
- Guðmundsson MT, Högnadóttir TH (2007) Volcanic systems and calderas in the Vatnajökull region, central Iceland: constraints on crustal structure from gravity data. *J Geodyn* 43:153–169
- Guðmundsson MT, Milsom J (1997) Gravity and magnetic studies of the subglacial Grímsvötn volcano, Iceland: implications for crustal and thermal structure. *J Geophys Res* 102:7691–7704
- Guðmundsson MT, Sigmundsson F, Björnsson H, Högnadóttir TH (2004) The 1996 eruption at Gjalp, Vatnajökull ice cap, Iceland: efficiency of heat transfer, ice deformation and subglacial water pressure. *Bull Volcanol* 66:46–65
- Guðmundsson M, Zimanowski B, Jude-Eton TC, Oddsson B, Buttner R, Dellino P, Thordarson, T Larsen G (2009) Energy partitioning in the phreatomagmatic basaltic eruption of Grímsvötn in 2004. In: AGU. San Francisco, pp V11B–1952
- Guðmundsson M, Pedersen R, Vogfjörð K, Thorbjarnadóttir B, Jakobsdóttir S, Roberts MJ (2010) Eruptions of Eyjafjallajökull volcano, Iceland. *EOS* 91(21)
- Houghton BF, Wilson CJN, Del Carlo P, Coltelli M, Sable JE, Carey R (2004) The influence of conduit processes on changes in style of basaltic Plinian eruptions: Tarawera 1886 and Etna 122 BC. *J Volcanol Geotherm Res* 137:1–14
- Inman DL (1952) Measures for describing the size distribution of sediments. *J Sedimentary Res* 22(3):125–145
- Jakobsson SP, Guðmundsson MT (2008) Subglacial and intraglacial volcanic formations in Iceland. *Jökull* 58:179–196
- Jones JG (1966) Intraglacial volcanoes of south-west Iceland and their significance in the interpretation of the form of the marine basaltic volcanoes. *Nature* 212:586–588
- Jones JG (1970) Intraglacial volcanoes of the Laugarvatn region, southwest Iceland, II. *J Geol Soc Lond* 78:127–140
- Jude-Eton TC (2011) Eruption dynamics within an emergent subglacial setting: a case study of the 2004 eruption of Grímsvötn volcano, Iceland. Dept. GeoSciences, University of Edinburgh. PhD. Thesis: pp 300
- Larsen G (2002) A brief overview of eruptions from ice-covered and ice-capped volcanic systems in Iceland during the past 11 centuries: frequency, periodicity, and implications. *Geol Soc Spec Publ* 202(25):81–90
- Larsen G, Eiríksson J (2008) Holocene tephra archives and tephrochronology in Iceland—a brief overview. *Jökull* 58:229–250
- Larsen G, Guðmundsson MT, Björnsson H (1998) Eight centuries of periodic volcanism at the centre of the Iceland hotspot revealed by glacier tephrostratigraphy. *Geology* 26:943–946
- McNutt SR, Nishimura T (2008) Volcanic tremor during eruptions: temporal characteristics, scaling constraints on conduit size and processes. *JVGR* 178:10–18
- Metrich N, Sigurdsson H, Meyer PS, Devine JD (1991) The 1783 Lakagigar eruption in Iceland: geochemistry, CO₂ and sulfur degassing. *Contrib Mineral Petrol* 107:435–447
- Oddsson B (2007) The Grímsvötn eruption in 2004: dispersal and total mass of tephra and comparison with plume transport models. Inst. Earth Sci. Reykjavik, University of Iceland. MSc. Thesis: pp 130
- Pyle DM (1989) The thickness, volume and grain size of tephra fall deposits. *Bull Volcanol* 51:1–15
- Rose W, Self S, Murrow P, Bonadonna C, Durant A, Ernst G (2008) Nature and significance of small volume fall deposits at composite volcanoes: insights from the October 14, 1974 Fuego eruption, Guatemala. *Bull Volcanol* 70:1043–1067
- Sable JE, Houghton BF, Del Carlo P, Coltelli M (2006) Changing conditions of magma ascent and fragmentation during the Etna 122 BC basaltic Plinian eruption: Evidence from clast microtextures. *Journal of Volcanology and Geothermal Research* 158:333–354
- Sæmundsson K (1982) Calderas in the active volcanic areas of Iceland. In: Thorarinsdóttir H, Óskarsson OH, Steinthorsson S, Einarsson T (eds) *Fire*. Sögufelag, Reykjavík, pp 221–239, In Icelandic
- Schumacher R, Schmincke HU (1995) Models for the origin of accretionary lapilli. *Bull Volcanol* 56:626–639
- Schuman U et al (2010) Airborne observations of the Eyjafjalla volcano ash cloud over Europe during air space closure in April and May 2010. *Atmos Chem Phys Discuss* 46:22131–22218
- Sigmundsson F, Guðmundsson MT (2004) The Grímsvötn eruption, November 2004. *Jökull* 54:139–142
- Skilling IP (1994) Evolution of an englacial volcano: Brown Bluff, Antarctica. *Bull Volcanol* 56:573–591
- Smellie JL (2000) Subglacial eruptions. In: Sigurðsson H (ed) *Encyclopaedia of volcanoes*. Academic, San Diego, pp 403–418
- Smellie JL, Hole MJ (1997) Products and processes in Pliocene—recent, subaqueous to emergent volcanism in the Antarctic Peninsula: examples of englacial Surtseyan volcano construction. *Bull Volcanol* 58(8):626–646
- Sohn Y, Chough SK (1989) Depositional processes of the Suwolbong tuff ring, Cheju Island (Korea). *Sedimentology* 36:837–855
- Sohn YK, Chough SK (1992) The Ilchulbong tuff cone, Cheju Island, South Korea. *Sedimentology* 39(4):523–544
- Thorarinnsson S (1953) Some new aspects of the Grímsvötn problem. *J Glaciol* 2:267–274
- Thorarinnsson S (1964) Surtsey: the new island in the Atlantic. Viking, New York, p 63
- Thorarinnsson S (1974) *Votnin Strið*. Menningarssjodur, Reykjavík, p 254
- Thordarson TH, Höskuldsson Á (2008) Postglacial volcanism in Iceland. *Jökull* 58:197–228
- Thordarson T, Larsen G (2007) Volcanism in Iceland in historical time: volcano types, eruption styles and eruptive history. *J Geodyn* 43:118–152

- Thordarson TH, Self S (1993) The Laki (Skaftár Fires) and Grímsvötn eruptions in 1783–1785. *Bull Volcanol* 55:233–263
- Vogfjörð KS et al (2005) Forecasting and monitoring a subglacial eruption in Iceland. *Eos* 15(86):245–248
- Walker GPL, Croasdale R (1972) Characteristics of some basaltic pyroclasts. *Bull Volcanol* 35:303–317
- Waters AC, Fisher RV (1971) Base surges and their deposits: Capelinhos and Taal volcanoes. *J Geophys Res* 76:5596–5614
- Wolfe CJ, Bjarnason IT, VanDecar JC, Solomon SC (1997) Seismic structure of the Iceland mantle plume. *Nature* 385:245–247